Brain state and cortical layer-specific mechanisms underlying perception at threshold

Mitchell P. Morton[1,2], Sachira Denagamage[1,2], Isabel J. Blume[1], John H. Reynolds[7], Monika P. Jadi[1,2,3,5] and Anirvan S. Nandy[1,2,4,5,6]
[1]Department of Neuroscience, Yale University, New Haven, CT 06511
[2]Interdepartmental Neuroscience Program, Yale University, New Haven, CT 06511
[3]Department of Psychiatry, Yale University, New Haven, CT 06511
[4]Department of Psychology, Yale University, New Haven, CT 06511
[5]Wu Tsai Institute, Yale University, New Haven, CT 06511
[6]Kavli Institute for Neuroscience, Yale University, New Haven, CT 06511
[7]Systems Neurobiology Laboratories, The Salk Institute for Biological Studies, La Jolla, CA 92037
Correspondence: anirvan.nandy@yale.edu

ABSTRACT

Identical stimuli can be perceived or go unnoticed across successive presentations, producing divergent behavioral outcomes despite similarities in sensory input. We sought to understand how fluctuations in behavioral state and cortical layer and cell-class specific neural activity underlie this perceptual variability. We analyzed physiological measurements of state and laminar electrophysiological activity in visual area V4 while monkeys were rewarded for correctly reporting a stimulus change at perceptual threshold. Hit trials were characterized by a behavioral state with heightened arousal, greater eye position stability, and enhanced decoding performance of stimulus identity from neural activity. Target stimuli evoked stronger responses in V4 in hit trials, and excitatory neurons in the superficial layers, the primary feed-forward output of the cortical column, exhibited lower variability. Feed-forward interlaminar population correlations were stronger in hits. Hit trials were further characterized by greater synchrony between the output layers of the cortex during spontaneous activity, while the stimulus-evoked period showed elevated synchrony in the feed-forward pathway. Taken together, these results suggest that a state of elevated arousal and stable retinal images allow enhanced

processing of sensory stimuli, which contributes to hits at perceptual threshold.

INTRODUCTION

Physical properties of stimuli strongly influence perception such that low-intensity stimuli are detected infrequently. As intensity increases, detection probability remains low until some perceptual threshold is crossed, after which stimuli are perceived robustly. A psychometric function (1-3) mathematically describes this property of perception. Only within a narrow range around the perceptual threshold do stimuli lead to significant trial-to-trial perceptual variance. While many studies present stimuli at threshold (4-7), few have probed the laminar cortical microcircuit mechanisms that underlie successful or unsuccessful perception under these conditions (8, 9).

Prior studies have characterized how perceived stimuli trigger stronger information propagation from earlier visual areas to higher-order visual and frontal regions (4, 9). This information propagation and sensory processing are strongly influenced by brain states such as arousal and attention (8, 10). Arousal has long been recognized for its role in modulating cortical activity (11-13) and affecting performance in various sensory tasks (14-16). In visual area V4, a key intermediate region in the ventral visual processing stream (17-19), attention strongly modulates neural activity (20-23). Attention increases the firing rates of V4 neurons, enhances the reliability of individual neuron firing, and reduces correlated fluctuations among pairs of neurons (21, 24-26). Brain state dynamics impact both cortical and subcortical structures, contributing to behavior (27, 28). Fluctuations in attention are reflected in the on- and off-state dynamics of V4 ensembles, which have been shown to correlate with behavioral performance (29, 30).

The visual cortex has a columnar architecture in which multiple cell classes (31-35) across the cortical layers (18, 36) form distinct sub-populations. These sub-

54 populations have unique and stereotyped patterns of connectivity, thus forming a
55 canonical microcircuit that orchestrates the encoding and flow of information (37, 38).
56 Moreover, these sub-populations contribute uniquely to sensory processing and are
57 differentially modulated by brain states (25, 39-41). While it has been shown that
58 attentional modulation varies across cortical layers (39, 41-47), the role of these sub-
59 populations in attentive perception at threshold remains poorly understood. Moreover, the
60 influence of physiological states, which may be responsible for different outcomes at
61 threshold, on these sub-populations has not been studied in detail.

62 Here we examine the neural mechanisms that regulate perception at threshold.
63 We specifically focus on the columnar microcircuit mechanisms within area V4. We
64 hypothesized that minor fluctuations in behavioral state, such as arousal and visual
65 sensitivity, and in the activity of neural sub-populations across the layers of the visual
66 cortex, result in different perceptual outcomes at threshold. Specifically, we hypothesized
67 that output layer (II-III, V-VI) sub-populations, ones projecting to higher cortical areas and
68 subcortical structures, would show evidence of improved capacity for stimulus
69 representation during successful perception. We also hypothesized that such successful
70 events would be accompanied by improved information propagation throughout a cortical
71 column. We find that differences in behavioral states and lamina-specific neural states
72 characterize correct and incorrect trials at threshold and explain perceptual variability.
73

74 **RESULTS**

75 To study the neural dynamics responsible for determining whether a stimulus presented
76 at perceptual threshold is perceived, we analyzed behavioral and cortical layer-specific

neural data from area V4, collected while monkeys performed a cued attention task (39). Monkeys were trained to detect an orientation change in one of two Gabor stimuli that were presented concurrently at two spatial locations, and to report having seen the change by making an eye movement to the changed stimulus. Prior to a block of trials, monkeys were cued as to which of the two spatial locations was likely to undergo the orientation change (95% valid cue; presented at the start of each block). During a trial, “non-target” stimuli at a fixed reference orientation were repeatedly presented. Non-targets were turned on for 200ms at the two spatial locations, and then turned off for a variable interval (200-400ms). At a random time (1-5s, mean 3s) a “target” stimulus, differing in orientation from the non-targets, was presented at one of the locations. If the monkey reported having detected the orientation change by making an eye movement to the location of the target stimulus, it received a juice reward (Figure 1A, “hit” trial). If the monkey failed to detect the orientation change and instead continued to maintain fixation on the center of the monitor, it was not rewarded (Figure 1A, “miss” trial). In this study, we focused exclusively on trials in which the target stimulus was presented at the cued location (95% of trials). All figures relate exclusively to trials in which the change occurred at the cued location.

On each trial, the magnitude of the orientation change was drawn from a distribution that spanned multiple levels of difficulty. We fit the behavioral data with a logistic function (1) and defined the threshold condition as the orientation change that was closest to the 50% threshold of the fitted psychometric function for that session (Figure 1B, Methods; see Figure 1-figure supplement 2 for additional examples and Figure 1-figure supplement 3A-G for logistic fit parameters). We selected this subset of trials for

100 further analysis, since the constant target stimuli in these trials were equally likely to be
101 perceived or not perceived. Target presentation times were not different between hit and
102 miss trials (Figure 1-figure supplement 3H; $p=0.15$, Wilcoxon rank sum test). There was
103 a slight difference in threshold trial performance based on time in the session (Figure 1-
104 figure supplement 3I, $p<0.01$, permutation test). Performance in the middle of the
105 recording session (second and third quartiles) was higher than in the beginning and end
106 of the session (first and fourth quartiles). Monkeys initiated a median of 905 trials per
107 session (range: 651 to 1086).

108 While monkeys performed this task, single- and multi-unit activity and local field
109 potentials (LFPs) were recorded in area V4 using 16-channel linear array electrodes
110 (Plexon inc., Figure 1-figure supplement 1A-E). The array was inserted perpendicular to
111 the cortical surface and spanned the cortical layers. We used current source density
112 (CSD) analysis (48) to estimate the boundaries between the superficial (I-III), input (IV),
113 and deep (V-VI) cortical layers (Figure 1-figure supplement 1E-F), and assign individual
114 neurons their layer identity (39). Single units were classified as either broad-spiking
115 (putative excitatory neurons) or narrow-spiking (putative inhibitory neurons) on the basis
116 of their waveform width using previously published techniques (peak to trough duration;
117 Figure 1-figure supplement 1D; see Methods; 31, 39, 40, 49, 50). Eye position and pupil
118 diameter were also recorded (ISCAN ETL-200). When analyzing pupil diameter and eye
119 position data, we considered all trials in the threshold condition in which the change
120 occurred at the cued location, regardless of whether the cued location was within the
121 receptive field of the recorded neurons. For all electrophysiological analyses, we only
122 considered trials in which the cued stimulus was within the receptive field of the recorded

neurons, and the stimulus change occurred at the cued location.

To assess the behavioral impact of variations in arousal and retinal image stability across trials at the threshold condition, we compared pupil diameter and microsaccade incidence across trial outcomes. Larger pupil diameter is thought to be a proxy for elevated alertness and arousal (8, 14, 15, 51-54). We found that hit trials were associated with larger pupil diameters compared to miss trials, both before and during non-target and target stimulus presentations (Figure 2A). We quantified this difference in the estimation statistics framework (55, 56) by comparing effect sizes and using bootstrapping to estimate uncertainty in the differences. We found that the mean of the distribution of pupil diameters associated with hit trials is greater than that associated with misses (Figure 2B; complementary null hypothesis testing results in Table 1). Prior work has shown that the optimal state for sensory performance occurs at intermediate levels of arousal, with states of low and hyper arousal associated with decreased performance (14-16, 57-60). In both hit and miss trials, the mean pupil diameter was close to the optimal arousal state for perceptual performance (Figure 2C; 15). The average differences in pupil diameter across hit and miss trials reflect differences within the optimal state of intermediate arousal. All results were held for individual animals (Figure 2-figure supplement 2A-C). Our results thus suggest that hits are more likely to occur during periods of greater arousal.

Microsaccades, small fixational eye movements of <1° in amplitude that occur during normal fixation, are associated with periods of decreased visual sensitivity due to unstable retinal images (61, 62). Microsaccades have been linked to suppressed neural responses in visual areas during perceptual tasks, impairing fine visual discrimination and behavioral performance (63, 64). We grouped trials in the threshold condition based on

whether a microsaccade occurred in a 400ms window preceding the onset of the target stimulus. Most trials with a pre-target microsaccade were misses, whereas the majority of trials without a microsaccade in this window were hits (Figure 2D; see Figure 2-figure supplement 2D for individual animal plots). There is a strong link between microsaccade direction and attention deployment (65-71). Consistent with previous reports we also find that microsaccades toward the attended stimulus were overrepresented in correct trials (Figure 2-figure supplement 1A, upper left). Conversely, microsaccades towards the attended stimulus were underrepresented in incorrect trials (Figure 2-figure supplement 1A, lower left). There was a very low but statistically significant negative correlation between pupil diameter and microsaccade rate (Figure 2-figure supplement 1B, $r^2 = 0.006$, $p < 0.001$). Microsaccade rates and inter-microsaccade times are reported in Figure 2-figure supplement 1C-D. Overall, these results suggest that successful trials at threshold are significantly more likely to occur during a state of greater arousal and improved visual sensitivity.

Having established that hit trials are more likely to occur in states of elevated arousal and visual stability, we investigated whether hits are characterized by differential information processing in V4. We first examined the ability to discriminate target stimuli from non-target stimuli using the firing rates of single and multi-unit V4 neurons in each of the three identified cortical layers (superficial, input, and deep). A linear decoder could better discriminate targets from non-targets in hits compared to misses (Figure 3A; see Figure 3-Figure supplement 1 for individual animal plots), suggesting differences in firing rates across these trial types. This improved stimulus discriminability was consistent across all three layers (Figure 3A).

169 Elevated stimulus-evoked firing rates would indicate a stronger representation of
170 the stimulus that could cause this improved discriminability in hits. We compared the firing
171 rates of all neurons (single and multi-units) recorded in each cortical layer across hit and
172 miss trials. For non-target stimuli, firing rates were equivalent for hits and misses in both
173 the pre-stimulus (0-200ms before stimulus onset) and stimulus-evoked (60-260ms
174 following stimulus onset) periods (Figure 3B; see Figure 3-figure supplement 2 for
175 individual animal plots). For the target stimulus, firing rates were once again equivalent in
176 the pre-stimulus period, but hit trials were characterized by elevated firing across cortical
177 layers in the stimulus-evoked period (Figure 3C-D). Broad and narrow-spiking neurons in
178 both the input and deep layers respond more to target stimuli in hit trials, and trend
179 towards elevated firing rates in the superficial layers during hits (Figure 3E). The average
180 firing rate in response to target stimuli for each neuron is shown in Figure 3-figure
181 supplement 3A for both hit and miss trials. It is important to note that the stimuli presented
182 to the animals were identical for both hits and misses. Moreover, the responses to the
183 target stimuli occur early, and elevated firing in hits emerges at the time of expected V4
184 response latencies (70-100 ms; Figure 3-figure supplement 3C), and thus cannot be
185 attributed to elevated levels of firing due to subsequent saccade planning in these trials
186 (Figure 3-figure supplement 3B; expected >200ms; 72).

187 Variability in response reflects how reliably information is encoded by a neural
188 population. Lower baseline variability can enhance the ability of neurons to encode
189 stimulus differences. We calculated the Fano factor, a mean-normalized measure of trial-
190 to-trial variability in firing, for single-units in our population (Figure 4A; see Figure 4-figure
191 supplement 1 for individual animal plots). We find that broad-spiking units in the

192 superficial layer exhibited lower Fano factor during the pre-stimulus period in hit trials (0-
193 60ms before non-target stimulus onset, Figure 4B), indicating this population of neurons
194 fired more reliably when the animal correctly detected the orientation change. This was
195 not the case for broad-spiking neurons in other layers (Figure 4B) or narrow-spiking
196 neurons (Figure 4-figure supplement 2).

197 We next wanted to test how the relationship between spiking activity and LFPs
198 may differ across hits and misses. Spike-LFP synchrony can reflect cortical processing
199 and both within- and inter-areal coordination (73-75). We calculated the PPC (76), a
200 frequency-resolved measure of spike-LFP phase-locking, for single and multi-units
201 relative to their local LFP signal during the pre-stimulus period (0-200ms before non-
202 target stimulus onset, Figure 5A; see Figure 5-figure supplement 2 for individual animal
203 plots). We averaged PPC values at low (3-12Hz), medium (15-25Hz), and high (30-80Hz)
204 frequency bands (superficial & Input: Figure 5-figure supplement 1A-B; deep: Figure 5B
205 & Figure 5-figure supplement 1C). Deep layer neurons exhibit reduced low-frequency
206 phase-locking in hit trials than in misses (Figure 5B). This desynchronization during hits
207 is similar to prior reports of desynchronization due to the deployment of attention (26, 39).

208 Our results at the individual neuron or neural-sub-population levels suggest
209 enhanced processing of perceived stimuli. However, it is the concerted activity among
210 neural sub-populations that ultimately determine information flow through the laminar
211 cortical circuit. We turned to canonical correlation analysis (CCA) to investigate the
212 strength of feed-forward communication across layers (77). CCA has previously been
213 used to describe interactions among multiple cortical areas (78). We performed CCA on
214 each pair of layers: input to superficial, input to deep, and superficial to deep, where the

two elements in each pair correspond to the upstream and downstream layers respectively (Figure 6A). We refer to the results of CCA as population correlations. Interlaminar feed-forward population correlations were higher in hits than in misses in both the pre-stimulus and stimulus-evoked periods (Figure 6B-C). This suggests that feed-forward information flow through the column is more effective in hits than in misses.

To further investigate interlaminar communication, we analyzed interlaminar synchrony as signatures of differential information flow between hit and miss trials. Spike-spike coherence (SSC) is a frequency-resolved measure of the degree to which two spike trains fluctuate together (26, 79). We measured interlaminar SSC for spike trains from pairs of cortical layers, each spike train being comprised of all recorded action potentials in a given layer (See Methods). We computed interlaminar SSC separately for hit and mis trials in both the pre-stimulus (0-200ms before non-target stimulus onset, Figure 7A) and non-target stimulus-evoked (60-260ms after non-target stimulus onset, Figure 7C) periods, matching the firing rates across hit and miss trials separately for the pre-stimulus and non-target stimulus-evoked conditions (see Figure 7-figure supplement 1 for individual animal plots). We averaged SSC for each pair of layers across three frequency bands, 3-12Hz, 15-25Hz, and 30-80Hz (Figure 7B and D).

Overall, hit trials have greater interlaminar SSC compared to misses at almost all frequencies (Figure 7B and D). In the pre-stimulus period, the strongest SSC difference between hits and misses was observed between the superficial and deep layers across all frequencies (Figure 7B, middle panel). This implies greater synchrony of the output layers of the cortex during hit trials. In contrast, this pattern was directionally the same during the non-target stimulus-evoked period, but stronger in the other layer pairs, with

238 greater SSC differences being found in pairs that involve the input layer (Figure 7D, top
239 and bottom). This may reflect a higher degree of stimulus-driven feed-forward information
240 propagation during hit trials. When comparing across time (pre-stimulus vs non-target
241 stimulus-evoked), layers, and frequency band, there was a significant interaction effect of
242 layer pair and time window (three-way ANOVA, $p = 0.0075$).

243 Finally, we sought to compare the predictive power of our results on the monkey's
244 perceptual performance. We created a generalized linear model (GLM) to regress
245 behavioral outcome from the pupil diameter, number of microsaccades in the pre-target
246 window, and average target-evoked multi-unit firing rate in each of the three layers (see
247 Methods; 80). Other reported measures (Fano factor, PPC, interlaminar population
248 correlations, and SSC) that we could not estimate reliably on a single trial basis were not
249 considered in the GLM analysis. Pre-target microsaccades were by far the strongest
250 predictor of performance ($weight = -1.3116$; $p = 6.0757e-08$). Input layer firing rate
251 also significantly predicted perception ($weight = 0.3276$; $p = 0.020068$). Superficial
252 firing rate, deep firing rate, and pupil diameter were not significant predictors (Table 2, all
253 $p > 0.5$). This indicates that, among the variables that we could estimate reliably on a
254 single trial basis, stable retinal images in the pre-target window are critical for behavioral
255 performance, and elevated firing in the input layer is the most reliable physiological
256 signature of a perceived stimulus. GLM fit parameters can be found in Table 3.

257 **DISCUSSION**

258 We investigated the physiological processes responsible for variable behavioral
259 outcomes at perceptual threshold. Controlling for *both* the attentive instruction (thus
260 minimizing large-scale attentional effects) and the stimulus condition that elicited

261 performance at a threshold level allowed us to examine the physiological and neural
262 correlates that underlie correct versus incorrect behavioral outcomes. While this study
263 cannot disentangle the independent roles of behavioral state fluctuations and neural
264 fluctuations in determining behavioral outcomes, evidence suggests that differences in
265 both are associated with hits. We found multiple lines of evidence which suggest that a
266 state of higher arousal and eye-position stability and the accompanying enhanced
267 processing of visual stimuli contributes to accurate perception in hit trials (Figure 8).

268 Pupil diameter is elevated in hit trials (Figure 2A-C; Figure 8A), and prior studies
269 have shown that pupil diameter is strongly linked to arousal and alertness (51, 52, 54).
270 This provides evidence that a state of higher arousal may contribute to improved sensory
271 processing. The much lower hit rate in trials with a microsaccade preceding the target
272 (Figure 2D; Figure 8A) and our GLM analysis show that stability of retinal images is critical
273 for accurate discrimination at threshold. It is unlikely that these two measures are
274 reflecting the same phenomenon, as there is a very weak correlation between them over
275 the course of a trial (Figure 2-figure supplement 1B).

276 There is a strong link between oculomotor control and attentional deployment (81-
277 83). In this study, hits and misses differ in their behavioral responses, with hit trials being
278 characterized by a saccade to the target stimulus. Almost all of our neural results reflect
279 differences around the time of non-target stimulus presentations during which the
280 monkeys maintained fixation at the center of the screen and, therefore, were hundreds of
281 milliseconds prior to saccade planning and execution in the case of hit trials. Trials in
282 which saccades were made to non-target stimuli were excluded from analysis, as were
283 trials in which the monkey made a saccade to the target too soon after its presentation to

have been a behavioral response to stimulus perception (see Methods). The analysis of microsaccade occurrence focused on the window just before target stimulus presentation and before monkeys could begin oculomotor planning. Only the analysis of neural responses to target stimuli appears in conjunction with divergent oculomotor behavior between the hit (saccade) and miss (no saccade) trials. However, here too firing rates diverge much earlier, particularly in the input layer, than would be consistent with the effects of saccade planning (Figure 3-figure supplement 1B; 72).

Non-target stimulus contrasts were slightly different between hits and misses (mean: 33.1% in hits, 34.0% in misses, permutation test, $p = 0.02$), but the contrast of the target was higher in hits compared to misses (mean: 38.7% in hits, 27.7% in misses, permutation test, $p = 1.6\,e - 31$). Firing rates were normalized by contrast in Figure 3. In all other figures, we considered only non-target stimuli, which had very minor differences in contrast (<1%) across hits and misses. While we cannot completely rule out any other effects of stimulus contrast, the normalization in Figure 3 and minor differences for non-target stimuli should minimize them.

A body of evidence (See 84 for review), suggests that microsaccades directed toward a target stimulus reflect attention-related processing and performance (65-71). In our dataset, during the pre-target period, microsaccades towards the attended stimulus were overrepresented in correct trials (Figure 2-figure supplement 1A, upper left). Conversely, microsaccades towards the attended stimulus were underrepresented in incorrect trials (Figure 2-figure supplement 1A, lower left). Microsaccades directed towards the location of the eventual target may reflect elevated attentional deployment that can compensate for reduced sensitivity due to a higher incidence of microsaccades.

307 Our electrophysiological findings and their laminar patterns associated with hit
308 trials *within* a cued attention state mirror several previous findings that are associated
309 with the deployment of covert spatial attention. Attention has long been known to increase
310 firing rates in V4 (21, 25, 85), and there is evidence that this increase occurs in all cortical
311 layers in V4 (39). We find improved target vs non-target discriminability in hits (Figure 3A)
312 across all cortical layers. Additionally, elevated target-evoked firing rates in hits occur
313 across all layers in conjunction with elevated arousal (Figure 3B-D; Figure 8C). Attention
314 reduces the variability in the firing of V4 neurons, and this reduction is thought to
315 contribute to the improved information coding capacity of a population of neurons (24-26,
316 39, 86). The reduction in Fano factor among broad-spiking superficial-layer neurons in hit
317 trials mirrors the effects of attention (Figure 4). Multiple lines of evidence suggest broad-
318 and narrow-spiking correspond to putative excitatory and inhibitory neurons respectively.
319 Narrow-spiking neurons exhibit higher firing rates, which corresponds well with inhibitory
320 interneuron (31, 39, 40, 87-89). Repolarization times in broad-spiking neurons are also
321 longer, as they are in excitatory pyramidal neurons (40, 50, 90). Since these neurons are
322 putative projection neurons to downstream cortical areas, this reduction in Fano factor
323 may indicate increased reliability in stimulus encoding that could contribute to hits. Our
324 finding is also in agreement with previous reports of higher variability in representations
325 of unperceived stimuli in humans (91). Synchronous neural activity appears to modulate
326 perceptual and cognitive ability in a variety of contexts (92-95). We found that deep-layer
327 neurons exhibit less low-frequency phase-locking in hit trials (Figure 5). This is consistent
328 with prior studies that find an attention-mediated reduction in the power spectrum of the
329 spike-triggered-averaged LFP (93).

330 In examining interlaminar population synchrony, we found that hit trials were
331 characterized by stronger feed-forward interactions across the cortical column (Figure 6).
332 This state of improved inter-laminar information flow could be a result of neuromodulatory
333 or top-down processes that maintain the cortex in a state of sustained depolarization
334 corresponding to a state of higher arousal during hits (8, 15). Our examination of inter-
335 laminar synchrony revealed two interesting and complementary patterns: hits were
336 associated with greater coherence between the superficial and deep layers during
337 spontaneous activity in the pre-stimulus period (Figure 7A-B; Figure 8B); in contrast, we
338 found enhanced coherence between the input layer and both the output layers (superficial
339 and deep) in the stimulus-evoked period during hits (Figure 7C-D; Figure 8C). Increased
340 superficial-deep coherence in the pre-stimulus period could be the result of the same
341 neuromodulatory or top-down processes. Increased synchrony between the input layer
342 and the output layers during the stimulus-evoked period provides further evidence of
343 stronger information propagation through the cortical circuit, and hence with improved
344 stimulus detection (96). In contrast to broad global synchrony or local correlated
345 fluctuations, which may signal a default state of minimal processing or decreased
346 information coding capacity (26, 97-99), these patterns of interlaminar coherence that we
347 found suggest that successful perception at threshold is mediated by pathway-specific
348 modulation of information flow through the laminar cortical circuit.

349 Prior studies showing decreased correlations under attention typically do not
350 contain laminar information (24, 26) or only consider decreased correlations within a layer
351 (39). In contrast, the correlation and synchrony analyses presented here are interlaminar,

352 which we expect could reflect improved information processing in a column, similar to
353 principles of communication across areas (78).

354 Taken together, our results provide insight about how information about a
355 threshold stimulus may successfully propagate through a cortical column and influence
356 sensory perception. Lower baseline variability among broad-spiking superficial layer
357 neurons and decreased low-frequency synchronous activity in the deep layers could be
358 indicative of improved capacity to encode sensory information. Higher target-evoked firing
359 rates and elevated interlaminar synchrony could enhance the propagation of this encoded
360 signal. These results associate pre-stimulus baseline state differences with enhanced
361 cortical processing in the stimulus-evoked period.

362 Several studies have examined how information flow differs for perceived and
363 unperceived stimuli at a more macroscopic scale (4, 9). van Vugt et al. (9) recorded from
364 three brain regions, V1, V4, and dorsolateral prefrontal cortex (dlPFC), while a monkey
365 performed a stimulus detection task at threshold. Their work supports the model that
366 feedforward propagation of sensory information from the visual cortex to the PFC causes
367 a non-linear “ignition” of association areas resulting in conscious perception (100).
368 Herman et al. (4) found that conscious human perception triggers a wave of activity
369 propagation from occipital to frontal cortex while switching off default mode and other
370 networks. Our study provides insight into the functions of the cortical microcircuit at the
371 columnar level that could reflect these large-scale sweeping activity changes in
372 perception.

373 Overall, we identified substantial layer-specific differences in cortical activity
374 between hits and misses at perceptual threshold, leading to the following conceptual

375 model (Figure 8). During spontaneous activity, the state of elevated arousal and eye
376 position stability during hits (Figure 8A) is manifested by increased interlaminar synchrony
377 between the superficial and deep layers (Figure 8B, thicker orange arrows), which we
378 propose is due to top-down influences. We predict that decreased firing variability in
379 broad-spiking neurons in the superficial layer is caused by a lower variability in membrane
380 potential closer to the action potential threshold among these neurons (Figure 8B, inset).
381 Elevated feed-forward propagation in the stimulus-evoked period (Figure 8C) and a
382 membrane potential closer to action potential threshold could both contribute to higher
383 firing rates in the output layers of the cortex (Figure 8C, inset), and are indicative of
384 greater fidelity of stimulus processing in hits. These physiological differences in the
385 laminar microcircuit likely contribute to successful perceptual discrimination at threshold.

386 **MATERIALS & METHODS**

387 **Surgical Procedures**

388 Surgical procedures have been described in detail previously (39, 101, 102). In brief, an
389 MRI compatible low-profile titanium chamber was placed over the pre-lunate gyrus, on
390 the basis of preoperative MRI in two rhesus macaques (right hemisphere in Monkey A,
391 left hemisphere in Monkey C). The native dura mater was then removed, and a silicone
392 based optically clear artificial dura (AD) was inserted, resulting in an optical window over
393 dorsal V4 (Figure 1-figure supplement 1A, B). Antibiotic (amikacin or gentamicin) soaked
394 gauzed was placed in the chamber between recording sessions to prevent bacterial
395 growth. All procedures were approved by the Institutional Animal Care and Use
396 Committee and conformed to NIH guidelines.

397

398 **Electrophysiology**

399 At the beginning of each recording session a plastic insert, with an opening for targeting
400 electrodes, was lowered into the chamber and secured. This served to stabilize the
401 recording site against cardiac pulsations. Neurons were recorded from cortical columns
402 in dorsal V4 using 16-channel linear array electrodes ('laminar probes', Plexon Inc.,
403 Plexon V-probe). The laminar probes were mounted on adjustable X-Y stages attached
404 to the recording chamber and positioned over the center of the pre-lunate gyrus under
405 visual guidance through a microscope (Zeiss Inc., Figure 1-figure supplement 1C). This
406 ensured that the probes were maximally perpendicular to the surface of the cortex and
407 thus had the best possible trajectory to make a perpendicular penetration down a cortical
408 column. Across recording sessions, the probes were positioned over different sites along
409 the center of the gyrus in the parafoveal region of V4 with receptive field (RF)
410 eccentricities between 2 and 7 degrees of visual angle. Care was taken to target cortical
411 sites with no surface micro-vasculature, with surface micro-vasculature used as reference
412 so that the same cortical site was not targeted across recording sessions. The probes
413 were advanced using a hydraulic microdrive (Narishige Inc.) to first penetrate the AD and
414 then through the cortex under microscopic visual guidance. Probes were advanced until
415 the point that the top-most electrode (toward the pial surface) registered local field
416 potential (LFP) signals. At this point, the probe was retracted by about 100-200 μm to
417 ease the dimpling of the cortex due to the penetration. This procedure greatly increased
418 the stability of the recordings and increased the neuronal yield in the superficial
419 electrodes.

The distance from the tip of the probes to the first electrode contact was either 300 μm or 700 μm. The inter-electrode distance was 150 μm, thus minimizing the possibility of recording the same neural spikes in adjacent recording channels. Electrical signals were recorded extracellularly from each channel. These were then amplified, digitized and filtered either between 0.5 Hz and 2.2 kHz (LFPs) or between 250 Hz and 8 kHz (spikes) and stored using the Multichannel Acquisition Processor system (MAP system, Plexon Inc.). Spikes and LFPs were sampled at 40 and 10 kHz respectively. LFP signals were further low-pass filtered with a 6th order Butterworth filter with 300Hz cut-off and down-sampled to 1 kHz for further analysis. Spikes were classified as either multi-unit clusters or isolated single units using the Plexon Offline Sorter software program. Single units were identified based on two criteria: (a) if they formed an identifiable cluster, separate from noise and other units, when projected into the principal components of waveforms recorded on that electrode and (b) if the inter-spike interval (ISI) distribution had a well-defined refractory period. Single-units were classified as either narrow-spiking (putative interneurons) or broad-spiking (putative pyramidal cells) based on methods described in detail previously (25, 39). Specifically, only units with waveforms having a clearly defined peak *preceded* by a trough were potential candidates. The distribution of trough-to-peak duration was clearly bimodal (Hartigan's Dip Test, $p = 0.012$) (103). Units with trough-to-peak duration less than 225 μs were classified as narrow-spiking units; units with trough-to-peak duration greater than 225 μs were classified as broad-spiking units (Figure 1-figure supplement 1D; teal=narrow, gold=broad).

Data was collected over 32 sessions (23 sessions in Monkey A, 9 in Monkey C), yielding a total of 413 single units (146 narrow-spiking, 267 broad-spiking) and 296 multi-

443 unit clusters. Per session unit yield was considerably higher in Monkey C compared to
444 Monkey A, resulting in a roughly equal contribution of both monkeys toward the population
445 data.
446
447 **Task, Stimuli and Inclusion Criteria**
448 Stimuli were presented on a computer monitor placed 57 cm from the eye. Eye position
449 was continuously monitored with an infrared eye tracking system (ISCAN ETL-200). Trials
450 were aborted if eye position deviated more than 1° (degree of visual angle, 'dva') from
451 fixation. Experimental control was handled by NIMH Cortex software
452 (http://www.cortex.salk.edu/). Eye-position (all sessions) and pupil diameter (18/32
453 sessions) data were concurrently recorded and stored using the MAP system.
454 *Receptive Field Mapping*: At the beginning of each recording session, neuronal
455 RFs were mapped using subspace reverse correlation in which Gabor (eight orientations,
456 80% luminance contrast, spatial frequency 1.2 cycles/degree, Gaussian half-width 2°) or
457 ring stimuli (80% luminance contrast) appeared at 60 Hz while the monkeys maintained
458 fixation. Each stimulus appeared at a random location selected from an 11x11 grid with
459 1° spacing in the appropriate visual quadrant. Spatial receptive maps were obtained by
460 applying reverse correlation to the evoked local field potential (LFP) signal at each
461 recording site. For each spatial location in the 11x11 grid, we calculated the time-
462 averaged power in the stimulus evoked LFP (0-200ms after each stimulus flash) at each
463 recording site. The resulting spatial map of LFP power was taken as the spatial RF at the
464 recording site. For the purpose of visualization, the spatial RF maps were smoothed using
465 spline interpolation and displayed as stacked contours plots of the smoothed maps

466 (Figure 1-figure supplement 1G). All RFs were in the lower visual quadrant (lower-left in
467 Monkey A, lower-right in Monkey C) and with eccentricities between 2 and 7 dva.

468 *Current Source Density Mapping*: In order to estimate the laminar identity of each
469 recording channel, we used a current source-density (CSD) mapping procedure (48).
470 Monkeys maintained fixation while 100% luminance contrast ring stimuli were flashed
471 (30ms) centered at the estimated RF overlap region across all channels. The size of the
472 ring was scaled to about three-quarters of the estimated diameter of the RF. CSD was
473 calculated as the second spatial derivative of the flash-triggered LFPs (Figure 1-figure
474 supplement 1E). The resulting time-varying traces of current across the cortical layers
475 can be visualized as CSD maps (Figure 1-figure supplement 1F; maps have been
476 spatially smoothed with a Gaussian kernel for aid in visualization). Red regions depict
477 current sinks in the corresponding region of the cortical laminae; blue regions depict
478 current sources. The input layer (Layer 4) was identified as the first current sink followed
479 by a reversal to current source. The superficial (Layers 1-3) and deep (Layers 5-6) layers
480 had opposite sink-source patterns. LFPs and spikes from the corresponding recording
481 channels were then assigned to one of three layers: superficial, input or deep.

482 *Attention task*: In the main experiment, monkeys had to perform an attention-
483 demanding orientation change-detection task (Figure 1A). While the monkey maintained
484 fixation, two achromatic Gabor stimuli (orientation optimized per recording session,
485 spatial frequency 1.2 cycles/degree, Gaussian halfwidth 2 degrees, 6 contrasts randomly
486 chosen from an uniform distribution of luminance contrasts, Monkey A: $contrast =$
487 $[10, 18, 26, 34, 42, 50\%]$, Monkey C: $contrast(8\ sessions) = [20, 28, 36, 44, 52, 60\%]$ or
488 $contrast(1\ session) = [30,40,50,60,70,80\%]$) were flashed on for 200 ms and off for a

variable period chosen from a uniform distribution between 200-400 ms. One of the Gabors was flashed at the receptive field overlap region, the other at a location of equal eccentricity across the vertical meridian. The range of stimulus contrasts was the same at both locations. At the beginning of a block of trials, the monkey was spatially cued ('instruction trials') to covertly attend to one of these two spatial locations. During these instruction trials, the stimuli were only flashed at the spatially cued location. No further spatial cue was presented during the rest of the trials in a block. At an unpredictable time drawn from a truncated exponential distribution (minimum 1 s, maximum 5 s, mean 3 s), one of the two stimuli changed in orientation. The monkey was rewarded for making a saccade to the location of orientation change. The monkey was rewarded for only those saccades where the saccade onset time was within a window of 100-400 ms after the onset of the orientation change. The orientation change occurred at the cued location with 95% probability and at the uncued location with 5% probability ('foil trials'). We controlled task difficulty by varying the degree of orientation change (Δ_{ori}), which was randomly chosen from one of the following: 1, 2, 3, 4, 6, 8, 10 and 12°. The orientation change in the foil trials was fixed at 4°. These foil trials allowed us to assess the extent to which the monkey was using the spatial cue, with the expectation that there would be an impairment in performance and slower reaction times compared to the case in which the change occurred at the cued location. If no change occurred before 5s, the monkey was rewarded for maintaining fixation ('catch trials', 13% of trials). We refer to all stimuli at the baseline orientation as 'non-targets' and the stimulus flash with the orientation change as the 'target'. Monkeys initiated a median of 905 trials (range of 651 to 1086).

Inclusion criteria: Of the 413 single units, we included only a subset of neurons that were visually responsive for further analysis. For each neuron we calculated its baseline firing-rate for each attention condition (attend into RF [‘attend-in’ or ‘IN’], attend away from RF [‘attend-away’ or ‘AWAY’]) from a 200ms window before a stimulus flash. We also calculated the neuron’s contrast response function for both attention conditions (Figure 1-figure supplement 1H). This was calculated as the firing rate over a window between 60-200 ms after stimulus onset and averaged across all stimulus flashes (restricted to non-targets) of a particular contrast separately for each attention condition. A neuron was considered visually responsive if any part of the contrast response curves exceeded the baseline rate by 4 standard deviations for both attention conditions. This left us with 274 single units (84 narrow-spiking, 190 broad-spiking) and 217 multi-unit clusters for further analysis.

Data analysis

Behavioral Analysis: For each orientation change condition Δ_{ori}, we calculated the hit rate as the ratio of the number of trials in which the monkey correctly identified the target by making a saccadic eye-movement to the location of the target over the number of trials in which the target was presented. The hit rate as a function of Δ_{ori}, yields a behavioral psychometric function (Figure 1B). We performed this analysis independently for each recording day for each monkey, yielding a similar but distinct psychometric function for every session. Psychometric functions were fitted with a smooth logistic function (1). Error bars were obtained by a jackknife procedure (20 jackknives, 5% of trials left out for each jackknife). Performance for the foil trials were calculated similarly as the

hit rate for trials in which the orientation change occurred at the un-cued location (Figure 1B, square symbol). When fitting the psychometric function, we did not include the contrast of the target stimulus as a variable, and fits were calculated by including trials with target stimuli of all tested contrasts. For each fitted psychometric function in both the attend-in and attend-away conditions, we calculated the threshold of the fitted logistic function (i.e. the Δ_{ori} at which performance was mid-way between the lower and upper asymptotes). Because the threshold of the fitted function always lies somewhere on the axis of Δ_{ori}, but not exactly at an orientation change presented to the subject, we then defined the threshold condition as the subset of trials in which the orientation change of the target stimulus was closest to the threshold of the fitted function (Figure 1B). We restricted further analysis to this threshold condition. For this threshold condition we identified the trials in which the monkey correctly identified the target as 'hit' trials and those in which the monkey failed to identify the target as 'miss' trials. Analysis of behavior, pupil diameter, and microsaccades was conducted on both the attend-in and attend-away conditions; all electrophysiological analysis was applied only to the attend-in condition.

To compare the effect of target timing across hits and misses, we determined the time between trial initiation and target presentation in all trials in the threshold condition. For comparison purposes, the contrast values of all target and non-target stimuli presented in the threshold condition were compared in hit and miss trials using a permutation test.

Pupil Diameter: The raw pupil diameter measurements from the infrared eye-tracking system could differ across days due to external factors such as display monitor illumination. To control for this, we normalized the raw data by a Z-score procedure

557 separately for each session (using the mean and standard deviation of all measurements
558 during the session). We analyzed normalized pupil diameter traces for hit and miss trials
559 in the threshold condition, over a time window from 100 ms before to 100 ms after all
560 stimulus presentations (non-target and target), excluding the first stimulus presentation in
561 a trial. The first stimulus was excluded to avoid pupil diameter changes due to the pupillary
562 near response caused by acquiring fixation (104). The pupil diameter was averaged over
563 this time period and compared across conditions using bootstrap estimation and *t*-test.
564 Distribution violin plots were generated using kernel density estimation (105)
565 (bandwidth(hit) = 0.0801, bandwidth(miss) = 0.0648). When analyzing pupil diameter, we
566 did not include the contrast of the target and non-target stimuli as a variable, and all
567 analyses were performed including by including stimuli of all tested contrasts.

568 *Microsaccade Analysis:* Saccadic eye-movements were detected using ClusterFix
569 (106). We identified microsaccades by filtering for eye movements with amplitudes
570 between 0.1 and 1 degree of visual angle. We then split all trials in the threshold condition
571 into two groups: those in which a microsaccade was detected in the 400ms preceding the
572 target stimulus presentation, and those without a detected microsaccade. We calculated
573 the hit rate for trials within those two groups. For all trials in which a target stimulus was
574 presented at the attended location, we determined the direction of all microsaccades in
575 the 400ms period preceding target presentation, relative to both the attended and
576 unattended stimuli. The relative microsaccade direction was defined as the angle
577 between two vectors: the one defined by the eye positions at the beginning and end of
578 the microsaccade, and the vector from the initial eye position to the center of the stimulus
579 (calculated separately for attended and unattended stimuli). Relative microsaccade

580 directions were grouped into 12 bins from 0-360°. The distribution of relative
581 microsaccade directions were calculated separately for correct and incorrect trials,
582 relative to both the attended and unattended stimuli (Figure 2-figure supplement 1A).

583 We next created a null distribution of relative microsaccade direction. This was
584 done by pooling together microsaccades from correct and incorrect trials and then
585 sampling with replacement from this pooled data (bootstrap procedure (107); 1000
586 samples). The number of microsaccades chosen for each sample was the same as the
587 number in correct or incorrect trials respectively. These bootstrapped samples were used
588 to create 99.5% confidence intervals for the count of microsaccades expected in each of
589 the 12 bins. A bin was considered significantly different from chance if it's true count fell
590 outside this confidence interval.

591 We calculated microsaccade rate for an entire trial by dividing the total number of
592 detected microsaccades in the whole trial by the trial length (4592 total trials). The
593 Pearson correlation between microsaccade rate and mean normalized pupil diameter
594 (see above) for the trial was calculated for all trials with pupil diameter data, regardless
595 of trial type or outcome (Figure 2-figure supplement 1B). Not pictured in Figure 2-figure
596 supplement 1B but included in correlation analysis were trials with a mean normalized
597 pupil diameter greater than 2 or less than -2 (~4% of trials). Only 4 of these trials were
598 longer than 1 s, out of which 2 trials contained detected microsaccades. The mean pupil
599 diameter in these trials is shown in Figure 2-figure supplement 1B inset. Inter-
600 microsaccade time was calculated as the time between microsaccade onset of
601 microsaccades detected in the same trial. 4% of microsaccades separated by >538 ms
602 are excluded from Figure 2-figure supplement 1D as they were more than 1.5x the

interquartile range above the third quartile. When analyzing microsaccades, we did not include the contrast of the target and non-target stimuli as a variable, and all analyses were performed including by including stimuli of all tested contrasts.

Decoding Analysis: For each single- or multi-unit neuron, we extracted spike counts from 60-260ms following all non-target or target stimulus onsets in the threshold condition. Using these spike counts, we fit a Poisson distribution to estimate the mean firing rate for each neuron in each of four stimulus conditions (non-targets and targets in hit and miss trials). Responses to stimuli of all contrasts were pooled together to create the Poisson fit. We then created a pseudo-population of neurons in each layer. We generated spike counts drawn from the fitted Poisson distributions to create synthetic spike counts for target and non-target stimuli in hits and misses separately (1000 repeats). We used linear discriminant analysis (LDA) to decode target from non-target stimuli. Decoders were trained separately for hit and miss trials. The procedure was repeated for a 20-fold cross-validation. We calculated the chance performance by training the decoder on data generated from all trials in the threshold condition (both hits and misses) and with shuffled labels (target or non-target).

Firing Rate: Firing rates were normalized per neuron to that neuron's maximum stimulus-evoked response to each contrast before being combined across contrasts and trial types. PSTH of firing rates were calculated in 30ms bins shifted in 5ms increments. For each tested contrast level, we calculated each neuron's maximum average firing rate in any bin from 0-260ms after stimulus onset in hit and miss trials together. We divided all bins in the entire PSTH for that contrast by this maximum firing rate to obtain the normalized firing rate for each contrast. We then combined PSTHs across contrasts and

split the data between hit and miss trials. We averaged stimulus-evoked firing rates from 60-260ms following non-target or target stimulus presentations. We used bootstrapped estimation to compare firing rates in hit and miss trials in a paired comparison. This was done for all single and multi-unit clusters, as well as broad- and narrow-spiking single-units in each layer. Firing rates were also compared across hit and miss trials by paired *t*-test for each group. To calculate the time of firing rate divergence, we compared the difference in each single neuron or multi-unit firing rate in the two conditions over time. At each time point, we performed a Wilcoxin rank-sum test comparing the firing rates across hits and misses, and defined the divergence point as the first time the firing rates were significantly different. Divergence was calculated separately for each layer. To determine the time at which firing rates rose above baseline levels, we used bootstrapping to estimate 95% confidence intervals for each neuron's pre-stimulus firing rate (0-100 ms before target or non-target stimulus onset). We then calculated the target PSTH for each neuron in 30ms bins shifted in 5ms increments. We defined the response latency as the first time bin in which the neuron's firing rate in the PSTH exceeded the upper limit of the 95% confidence interval of baseline firing. We calculated the response latency independently for hit and miss trials for each neuron.

Fano factor: Trial-to-trial variability was estimated by the Fano factor, which is the ratio of the variance of the spike counts across trials over the mean of the spike counts for each broad and narrow-spiking single unit. The Fano factor was calculated over non-overlapping 20ms time bins in a window from 200ms prior to each non-target flash onset to 200ms after each non-target flash onset for hit and miss trials in the threshold condition.

To compare across conditions, we calculated the Fano factor modulation index (MI), defined as

$$\mathrm{MI} = \frac{FF_{hit} - FF_{miss}}{FF_{hit} + FF_{miss}}$$

where FF_{hit} and FF_{miss} represent the Fano factor for a given unit in hit and miss trials respectively at each point in time with respect to non-target stimulus onset. The Fano factor MI was averaged from 0-60ms prior to non-target stimulus onset (disregarding stimulus contrast) and compared across trial types in the threshold condition for each sub-population.

Pairwise Phase Consistency (PPC): We calculated PPC (76) for single and multi-units in the non-target pre-stimulus period (0-200ms preceding onset regardless of stimulus conrrast) in trials in the threshold condition. Although PPC is unbiased by spike count, we set a threshold of 50 spikes for analysis so that only units with enough spikes for a reliable estimate of PPC were included (superficial: $n = 26$, input: $n = 41$, deep: $n = 64$). LFP phase was calculated using Morlet wavelets. PPC for each unit was calculated for the phase of the LFP recorded on the same channel and averaged in three frequency bands (3-12 Hz, 15-25 Hz, and 30-80 Hz). PPC was calculated separately for hit and miss trials and compared across trial outcomes by t-test, corrected for multiple comparisons.

Canonical Correlation Analysis (CCA): We used CCA (78, 108) to capture the correlation between layers at different time periods and with different amounts of temporal delays. We considered all possible combinations of pairs of layers. We took two windows of activity, one in each layer, in either the pre-stimulus period (0-200ms before non-target stimulus onset) or stimulus-evoked period (60-260ms after non-target stimulus onset),

including responses to stimuli of all contrasts. Window length was 50ms and the window was advanced in 10ms steps. The activity within each window was then binned using 10ms bins. We reported correlation associated with the first two canonical pairs, and calculated it separately for hit and miss trials. For each pair of layers, we limited CCA to sessions in which there were at least two neurons recorded in both layers. Feed-forward (FF) layer pairs were defined as follows: input to superficial, input to deep, and superficial to deep. The correlations along the FF signaling pathways (C_{FF}) were calculated as the mean correlation at positive delays:

$$C_{FF} = \frac{\sum_{dt>0} C(t, dt)}{N_{dt>0}}$$

where t is the time following response onset, dt is the inter-laminar delay involved between windows from two layers, $C(t, dt)$ is the corresponding correlation. $N_{dt>0}$ is the number of positive delays investigated. The values in Figure 6B correspond to C_{FF} in each session.

Spike-spike coherence (SSC): For each recording session, all spikes recorded from visually responsive single and multi-units in each layer were combined into a single spike train for that layer (layer multi-unit). Separately for both the pre-stimulus and non-target stimulus-evoked periods, we randomly deleted spikes from the layer multi-unit with a higher firing rate so that the firing rates were matched across hit and miss trials. SSC was calculated for each of the three possible pairs of layer multi-units in each session for both the pre-stimulus (0-200 ms preceding stimulus onset) and non-target stimulus evoked period (60-260 ms following non-target stimulus onset, including all stimuli regardless of contrast) separately for hit and miss trials using Chronux (NW = 1; K = 1; http://chronux.org) (77, 79). To control for differences in firing rates across hit and miss

trials we used a rate matching procedure (26). For estimation statistics, interlaminar SSC values was calculated for each frequency and subsequently averaged across three frequency bands: 3-12 Hz, 5-15 Hz, and 30-80 Hz and compared across hit and miss trials for each pair of layers in each recording session. For null-hypothesis testing, we calculated the SSC modulation index, defined as

$$\mathrm{MI} = \frac{SSC_{hit} - SSC_{miss}}{SSC_{hit} + SSC_{miss}}$$

The SSC MI was calculated for each frequency and subsequently averaged across three frequency bands: 3-12 Hz, 5-15 Hz, and 30-80 Hz. MI values for each frequency band were compared to zero by t-test, Bonferroni corrected for multiple comparisons. We tested for interaction effects with a three-factor ANOVA, with frequency, pair of layers, and time window (pre or post stimulus) as factors. We calculated a shuffled distribution of SSC by shuffling the trial identities of the spikes in one of the layers in the pair. We then calculated SSC with the shuffled trial identities. This procedure was repeated 10 times to create the shuffled distribution.

GLM quantification: To compare how well our results can predict behavioral performance we fit a GLM to the response of the monkeys in trials in the threshold condition (80). We included five regressors in our analysis: (1) average pupil diameter during the trial, (2) number of microsaccades in the pre-target window (0-400ms before target stimulus onset), and average target-evoked multi-unit firing rate in the (3) superficial, (4) input, and (5) deep layers. We calculated the average target-evoked firing rate by averaging the firing rate of all single- and multi-units in a given layer 60-260ms after target stimulus onset in each trial. In order to be able to compare weights across regressors, each regressor was transformed into a z-score before being included in the

model. We fit the GLM using a logit link function, using the predictors to regress the categorical binary trial outcome (hit or miss). A total of 309 trials were included in the GLM. Stimulus contrast was not a variable in the GLM.

FIGURE LEGENDS

Figure 1. Orientation change detection task at perceptual threshold

(**A**) Schematic of task structure. The monkey initiated a trial by fixating on the center of the screen. Two Gabor stimuli (represented by oriented lines) were presented for 200 ms and then turned off for 200-400ms. This was repeated until, at an unpredictable time, one of the stimuli changed orientation. The monkey could report having seen the change by making an eye movement to the location of the target stimulus to receive a reward (hit trials). If the monkey failed to report the orientation change and maintained fixation on the center of the screen it was not rewarded (miss trials). Before a block of trials, the monkey was cued as to which stimulus was likely to undergo the change (95% valid cue). In 5% of trials the orientation change occurred at the other location (foil trials). Circles indicating the cued location and receptive field are drawn for figure reference only and were not presented during the task. (**B**) Example behavioral psychometric function from one recording session and attention condition. Behavioral performance (hit rate, circles) is presented as a function of orientation change. Data was fitted with a logistic function. The threshold condition, trials with performance halfway between the upper and lower asymptotes of the logistic function, is indicated by the orange box. Error bars represent standard deviation calculated with a jackknife procedure (20 jackknives). The square symbol indicates foil trial performance.

Figure 2. Hit trials have larger pupil diameter whereas microsaccades more often precede misses

(**A**) Normalized pupil diameter for hit and miss trials in the threshold condition. 0 ms corresponds to non-target and target stimulus onset. Mean +/- s.e.m. (**B**) Distribution of pupil diameter values associated with hit and miss trials. Pupil diameter was averaged from 100ms before to 100ms after non-target and target stimulus onset. Violin plots were generated using kernel smoothing (See Methods). Error bars represent 95% confidence intervals for the mean of each distribution, and the mean difference (blue, right axes). *Inset*: zoomed in view of the mean difference between hit and miss trials. Black bar represents a 95% confidence interval of the mean difference. Shaded region reflects the distribution of the bootstrapped estimation of the mean difference. (**C**) Histogram of mean pupil diameter around the time of non-target and target stimulus onset (calculated as in **B**). Orange and gray lines represent the mean pupil diameter for hit and miss trials respectively. (**D**) *Left:* Hit rate for trials with (387 trials) and without (*right*, 1336 trials) a microsaccade detected in the time window 0-400ms before target onset. *Right:* Bootstrapped estimation of the mean difference in hit proportion in trials with vs without a pre-target microsaccade. Same conventions as **2B**.

Figure 3. Target stimuli evoke higher firing rates in hit trials

Rows correspond to different layers (top=superficial, middle=input, bottom=deep). (**A**) Performance for decoding targets from non-targets from single-units and multi-units in each layer. Points in the left section of each plot show the decoding performance for each of the 20 different cross-validations. The right section for each layer shows the bootstrapped estimation of the difference between decoding performance between hits and misses. Half-violin plots show the bootstrapped distribution of the difference, and black dots and bars represent the mean and 95% confidence intervals of the difference in decoding performance. Chance levels, determined by shuffling target and non-target identity, were subtracted from the raw decoding performance values. (**B**) Non-target population (single and multi-unit) PSTH of visually responsive neurons for the hit (orange) and miss (dark-gray) trials in the threshold condition (mean +/- s.e.m). The horizontal black bar indicates the time and duration of stimulus presentation. (**C**) As in **B** but for target stimuli. The star indicates the time at which firing rates in the input layer first differ significantly between hit and miss trials. Vertical lines represent the mean time at which firing rates for each neuron rise above the 95% confidence interval of their baseline activity (see also Figure S3C). (**D**) Bootstrapped estimation of the paired mean difference in target stimulus-evoked firing rate between hit and miss trials in the time window 60-260ms (red dotted box in **C**) after target stimulus onset. Shaded regions represent the bootstrapped estimation of the paired mean difference in firing rate (hit - miss), and black lines are 95% confidence intervals. Plots include data from both single and multi-units, separated by layer (top= superficial, middle=input, bottom=deep). (**E**) As in **D**, bootstrapped estimation of the paired mean difference in firing rate for hit trials compared to miss trials in the target stimulus-evoked period, but only for single-units broken up by cell class (gold=broad, teal=narrow).

Figure 4. Broad-spiking neurons in the superficial layer have decreased variability in hit trials

(**A**) Rows correspond to different layers (top=superficial, middle=input, bottom=deep). The Fano factor of broad-spiking putative excitatory neurons for the hit and miss trials in the threshold condition (mean +/- s.e.m). There is a significant decrease in variability for the hit trials prior to stimulus onset only in the superficial layer. 0 ms corresponds to non-target stimulus onset. The average Fano factor within a 60ms time-window (red dashed box) prior to non-target stimulus onset is plotted in **B**. (**B**) *Top:* Fano factor modulation index for each broad-spiking neurons recorded in each layer, averaged in the 60ms preceding non-target stimulus onset. *Bottom:* Bootstrapped estimation of the mean difference of the Fano factor modulation index from zero in each of the three layers. Colored curves represent the estimated bootstrapped distribution. Black dots and lines reflect the mean and 95% confidence intervals of the distributions.

Figure 5. Deep layer neurons are phase-locked to low-frequency rhythms in miss trials
(**A**) Pairwise phase consistency (PPC) of single and multi-units in each layer to the local field potential (LFP) signal recorded from the same channel in hit and miss trials at threshold. PPC was calculated in the pre-stimulus period (0-200 ms before stimulus onset). Dashed red line indicates a PPC of 0, below which there is no consistent relationship between spikes and LFP phase. (**B**) Bootstrapped estimation plot for the paired mean difference in PPC for deep layer neurons over three frequency bands: 3-12Hz, 15-25Hz, 30-80Hz. Curves represent the bootstrapped distribution for the paired difference, and black dots and vertical lines represent the mean and 95% confidence intervals for the paired mean difference.

Figure 6. Hit trials are characterized by stronger feed-forward interlaminar population correlations
(**A**) CCA-based population correlation as a function of time and inter-laminar delay during the pre-stimulus and stimulus-evoked periods in hit and miss trials in an example session. (**B**) Mean feed-forward population correlation in each session. Color indicates the monkey (blue=monkey A, yellow=monkey C). (**C**) Bootstrapped estimation plot for the paired mean difference in population correlation for each pair of layers and time window (pre-stimulus or stimulus-evoked). Curves represent the bootstrapped distribution for the paired difference, and black dots and vertical lines represent the mean and 95% confidence intervals for the paired mean difference.

Figure 7. Greater interlaminar coherence in hit trials in the pre-stimulus and non-target stimulus-evoked periods
Rows correspond to different pairs of layers (*top*=superficial-input, *middle*=superficial-deep, *bottom*=input-deep). (**A**) Multi-unit interlaminar spike-spike coherence (SSC) calculated in the 200ms before non-target stimulus onset in hit and miss trials (solid lines, mean +/- s.e.m). Firing rates were matched across hit and miss trials. Dashed lines represent coherence calculated with shuffled trial identities (mean +/- s.e.m). (**B**) Bootstrapped estimation plot for the paired mean difference in SSC for each pair of layers averaged over three frequency bands : 3-12Hz, 15-25Hz, 30-80Hz. Curves represent the bootstrapped distribution for the paired difference, and black dots and vertical lines represent the mean and 95% confidence intervals for the paired mean difference. (**C**) Interlaminar spike-spike coherence in the non-target stimulus-evoked period (60-260ms after stimulus onset). Same conventions as in **A**. (**D**) Bootstrapped estimation plot for the paired mean difference in SSC for each pair of layers averaged over three frequency bands. Same conventions as **B**.

Figure 8. Conceptual model for stimulus processing at perceptual threshold
(**A**) Hit trials have a larger pupil diameter and fewer pre-target microsaccades, reflecting a state of increased arousal and greater eye position stability. Conversely, miss trials show decreased arousal and eye position stability. (**B**) In the spontaneous pre-stimulus period, hits are characterized by decreased variability in superficial layer broad-spiking neurons, which we hypothesize is reflective of lower membrane potential (V_m) variability (inset). Hit trials are also characterized by greater synchrony between the superficial and deep layers (indicated by thicker arrows), which could be reflecting a stronger top-down influence on the cortical column. (**C**) In the stimulus-evoked period there is greater interlaminar synchrony between pairs that include the input layer (represented by thicker arrows), which we propose reflects improved feed-forward propagation of information. We propose these state differences in hits contribute to elevated firing rates in response to target stimuli, particularly in the superficial layers (inset), resulting in a higher-fidelity output to downstream areas. E = excitatory; I = inhibitory; s = superficial; i = input; d = deep.

Figure 1-figure supplement 1. Laminar recordings in V4 (Modified from Nandy et a. (2017)).
(**A**) An artificial dura (AD) chamber is shown over dorsal V4 in the right hemisphere of Monkey A. The native dura mater was resected and replaced with a silicone based artificial dura, thereby providing an optically clear window into the cortex. Scale bar = 5mm. (**B**) An enlarged view of the boxed region in **A** clearly shows the sulci and the microvasculature. sts = superior temporal sulcus, lu = lunate sulcus, io = inferior occipital sulcus. Area V4 lies on the pre-lunate gyrus between the superior temporal and lunate sulci. Scale bar = 2mm. (**C**) Electrophysiology setup: a plastic stabilizer with a circular aperture is secured in place inside the chamber such that the aperture is centered over the pre-lunate gryus. A 16-channel linear array electrode (electrode spacing 150 μm) is positioned over the center of the gyrus and lowered into the cortex under microscopic guidance. The microvasculature pattern was used as a reference to target different cortical sites across recording sessions. (**D**) Example recording session in monkey C depicting 12 single unit waveforms (mean +/- s.e.m.) isolated along the cortical column. Teal waveforms correspond to narrow-spiking putative interneurons and gold waveforms correspond to broad-spiking putative excitatory units. (**E**) Stimulus triggered local field potentials (LFPs) obtained by flashing 30ms high contrast ring stimuli in the receptive field of a V4 cortical column. LFP traces averaged across all stimulus repeats are shown color-coded as being part of either the superficial (green), input (gray) or deep (pink) layers. Layer assignment was done after current source-density analysis. (**F**) Current source-density (CSD) calculated as the second spatial derivative of the stimulus triggered LFPs and displayed as a colored map. The x-axis represents time from stimulus onset; the y-axis represents cortical depth oriented such that the pial surface is at the top and the white matter is at the bottom. Red hues represent current sink, blue hues represent current source. The input layer is identified as the first current sink followed by a reversal to current source. The superficial and deep layers have the opposite sink-source pattern. The CSD map has been spatially smoothed for visualization. (**G**) Stacked contour plots show spatial receptive fields (RFs) mapped along each contact point in the laminar probe. The spatial receptive fields were obtained by applying reverse correlation to the LFP power evoked by sparse pseudo-random sequences of Gabor stimuli. The RFs are well aligned, indicating perpendicular penetration down a cortical column. Zero depth represents the center of the input layer as estimated from the CSD. (**H**) Contrast response functions – spikes rate as a function of stimulus contrast – are shown for 2 example units identified in a single recording session in Monkey A. Red and blue traces correspond to the attend-in to RF and attend-away from RF conditions respectively. The dotted lines represent the corresponding background firing-rates. The dashed lines are 4 standard deviations above baseline. A unit was considered as visually responsive, if the contrast response functions exceeded this threshold in both the attention conditions. Mean +/- s.e.m. Panels are reproduced from Nandy et al. (2017).

Figure 1-figure supplement 2. Additional psychometric function examples.
Example behavioral psychometric functions from 9 recording sessions in the attend in (red) and attend away (blue) conditions. Behavioral performance (circles) is presented as a function of orientation change. Data was fitted with a logistic function. The threshold of each fitted logistic function is indicated by the vertical dashed line. The square symbol indicates foil trial performance, and the star symbol indicates catch trial performance.

Figure 1-figure supplement 3. Psychometric function parameters.
(**A**) Distribution of the orientation threshold of the fitted psychometric functions in the attend-in (red solid) and attend-away (blue hatch) conditions for each recording session. The threshold of the sigmoid may not correspond exactly to an orientation change tested in the experiment. (**B**) Distribution of threshold orientation changes used as the threshold condition in the rest of this study (red=attend-in, blue=attend-away, circle=monkey A, plus=monkey C). (**C**) Distribution of slopes for the fitted psychometric functions (same conventions as **A**). (**D**) Distribution of guess rate for the fitted psychometric functions (same conventions as **A**). (**E**) Distribution of lapse rate for the fitted psychometric functions (same conventions as **A**). (**F**) Distribution of catch trial performance in each session (same conventions as **A**). (**G**) Performance on orientation-change matched regular trials (target presented at cued location) and foil trials (target presented at uncued location) for each session (same conventions as **B**). (**H**) Distribution of target presentation time for hit (orange) and miss (gray) trials. (**I**) Performance in threshold trials in each recording session split by quartiles (see Methods). Error bars represent standard deviation.

Figure 2-figure supplement 1. Microsaccades are preferentially directed towards the target in correct trials and have a slight correlation with pupil diameter

Data is presented for all trials, regardless of orientation change (not just the threshold condition). (**A**) The histograms represent the direction of microsaccades relative to the attended stimulus (left column) or unattended stimulus (right column) in correct (top row) and incorrect (bottom row) trials. Black lines represent the mean (solid) and 99.5% confidence interval (dashed) of the bootstrapped null distribution estimated by pooling correct and incorrect microsaccades. $*\,\mathrm{p} < 0.005$. *Inset:* Schematic for calculation of relative microsaccade direction. Microsaccade is represented by the gray arrow (**B**) Scatterplot of microsaccade rate versus mean normalized pupil diameter, shows a small but statistically significant relationship between the two quantities ($r^2 = 0.006$, $p < 0.001$). Each dot is color-coded by trial length. *Inset:* Histogram of mean pupil diameter for all trials, including those less than -2 or greater than 2 (red lines). Only four of the trials with pupil diameters less than -2 or greater than 2 had detected microsaccades. (**C**) Boxplot of microsaccade rates for all trials. (**D**) Boxplot of the time between microsaccades recorded in the same trial. 4% of microsaccades separated by more than 538ms were excluded as outliers (See Methods).

Figure 2-figure supplement 2. Single monkey pupil diameter and microsaccade data.

(**A**) Normalized pupil diameter for hit and miss trails in the threshold condition separated by monkey. 0 ms corresponds to non-target and target stimulus onset. Mean +/- s.e.m. (**B**) Distribution of pupil diameter values associated with hit and miss trials separated by monkey. Pupil diameter was averaged from 100ms before to 100ms after non-target and target stimulus onset. Violin plots were generated using kernel smoothing (See Methods). Error bars represent 95% confidence intervals for the mean of each distribution, and the mean difference (blue, right axes). (**C**) Histogram of mean pupil diameter around the time of non-target and target stimulus onset for each monkey (calculated as in **B**). Orange and gray lines represent the mean pupil diameter for hit and miss trials respectively. (**D**) Hit rate for trials with and without a microsaccade detected in the time window 0-400ms before target onset for each monkey.

Figure 3-figure supplement 1. Single monkey decoding performance

(**A**) Performance for decoding targets from non-targets from single-units and multi-units in the superficial layer for individual monkeys. Points in the left section of each plot show the decoding performance for each of the 20 different cross-validations. The right section for each layer shows the bootstrapped estimation of the difference between decoding performance in hits and misses. Half-violin plots show the bootstrapped distribution of the difference, and black dots and bars represent the mean and 95% confidence intervals of the difference in decoding performance. Chance levels, determined by shuffling target and non-target identity, were subtracted from the raw decoding performance values. (**B**) Same as **A** but for the input layer. (**C**) Same as **A** but for the deep layers.

Figure 3-figure supplement 2. Single monkey firing rate data

(**A**) Single monkey non-target population (single and multi-unit) PSTH of visually responsive neurons for the hit (orange) and miss (dark-gray) trials in the threshold condition (mean +/- s.e.m). (**B**) As in **A** but for target stimuli. Red box indicates the time window used for analysis in **3C.**

Figure 3-figure supplement 3. Firing rates for individual neurons and reaction time in threshold condition

(**A**) Target stimulus-evoked normalized firing rates in hit and miss trials for each recorded single and multi-unit cluster in hit and miss trials. Clusters are divided by layer: left=superficial, middle=input, right=deep. Related to **Figure 3B**. Each line represents the mean firing rate in response to target stimuli in hit and miss trials for a given unit. Data is color coded by unit type (gold=broad, teal=narrow, gray=multi-unit). See Methods for normalization method. (**B**) Mean reaction time (time from target stimulus onset to saccade onset) for hit trials in the threshold condition in both attend-in (red) and attend-away (blue) trials for each recording session. (**C**) Mean time at which single- and multi-unit firing rates rise significantly above pre-stimulus baseline in response to target stimuli in hit and miss trials. Mean +/- s.e.m.

Figure 4-figure supplement 1. Single monkey Fano factor data

Rows correspond to different layers (top=superficial, middle=input, bottom=deep) and columns correspond to monkeys. The Fano factor of broad-spiking putative excitatory neurons for the hit and miss trials in the threshold condition in each monkey (mean +/- s.e.m).

Figure 4-figure supplement 2. Narrow-spiking neurons do not have decreased variability in hit trials
Top: Fano factor modulation index for each narrow-spiking neurons recorded in each layer, averaged in the 60ms preceding non-target stimulus onset. *Bottom:* Bootstrapped estimation of the mean difference of the Fano factor modulation index from zero in each of the three layers. Colored curves represent the estimated bootstrapped distribution. Black dots and lines reflect the mean and 95% confidence intervals of the distributions.

Figure 5-figure supplement 1. Additional PPC data
(**A-B**) *Top:* Raw PPC values calculated for clusters recorded in the superficial (**A**) and (**B**) input layers in hit and miss trials, averaged into three frequency bands, 3-12 Hz, 15-25 Hz, and 30-80 Hz. PPC was calculated using the LFP recorded on the same channel as the spikes. *Bottom:* Bootstrapped estimation of the paired mean difference in PPC across hit and miss trials for each frequency band. Note that although there appears to be a difference in high-frequency PPC in the superficial layer, this population does not have significantly positive PPC in either condition, indicating that there is no phase-locking in either hits or misses. (**C**) Raw PPC values for neurons recorded in the deep layer in hit and miss trials, averaged into the same 3 frequency bands. Related to **Figure 5B**.

Figure 5-figure supplement 2. Single monkey PPC data
Rows correspond to different layers (top=superficial, middle=input, bottom=deep) and columns correspond to monkeys. Pairwise phase consistency (PPC) of single and multi-units in each layer to the local field potential (LFP) signal recorded from the same channel in hit (orange) and miss (gray) trials at threshold. PPC was calculated in the pre-stimulus period (0-200 ms before stimulus onset). Dashed red line indicates a PPC of 0, below which there is no consistent relationship between spikes and LFP phase.

Figure 7-figure supplement 1. Single animal interlaminar coherence
Rows correspond to different pairs of layers (*top*=superficial-input, *middle*=superficial-deep, *bottom*=input-deep). (**A**) Single monkey multi-unit interlaminar spike-spike coherence (SSC) calculated in the 200ms before non-target stimulus onset in hit and miss trials (solid lines, mean +/- s.e.m). Firing rates were matched across hit and miss trials. Dashed lines represent coherence calculated with shuffled trial identities (mean +/- s.e.m). (**B**) Interlaminar spike-spike coherence in the non-target stimulus evoked period in each monkey (60-260ms after stimulus onset). Same conventions as in **A**.

AUTHOR CONTRIBUTIONS

MPJ and ASN conceptualized the project. ASN collected the data and supervised the project. MPM analyzed the data, with assistance from SD and IB. MPM, SD, ASN, MPJ, and JHR wrote the manuscript.

ACKNOWLEDGEMENTS

This research was supported by NIH R01 EY021827 to JHR and ASN, NIH R01 EY032555, NARSAD Young Investigator Grant, Ziegler Foundation Grant, Yale Orthwein Scholar Funds & Lawrence Family Young Investigator Funds to ASN, NIH R01 EY034605 & NIH R00 EY025026 to MPJ, and by NEI core grants for vision research P30 EY019005 to the Salk Institute and P30 EY026878 to Yale University. MM was supported by training grants T32-NS007224 and T32-NS041228 to Yale University. We would like to thank Catherine Williams and Mat LeBlanc for their excellent animal care.

REFERENCES

1. N. Prins, F. A. A. Kingdom, Applying the Model-Comparison Approach to Test Specific Research Hypotheses in Psychophysical Research Using the Palamedes Toolbox. *Frontiers in Psychology* **9** (2018).
2. A. B. Watson, Probability summation over time. *Vision Research* **19**, 515-522 (1979).
3. F. A. Wichmann, N. J. Hill, The psychometric function: I. Fitting, sampling, and goodness of fit. *Perception & Psychophysics* **63**, 1293-1313 (2001).
4. W. X. Herman *et al.*, A Switch and Wave of Neuronal Activity in the Cerebral Cortex During the First Second of Conscious Perception. *Cerebral Cortex* **29**, 461-474 (2017).
5. H. Levitt, Transformed Up‐Down Methods in Psychoacoustics. *The Journal of the Acoustical Society of America* **49**, 467-477 (1971).
6. D. Pins, D. ffytche, The Neural Correlates of Conscious Vision. *Cerebral Cortex* **13**, 461-474 (2003).

7. D. Ress, D. J. Heeger, Neuronal correlates of perception in early visual cortex. *Nat Neurosci* **6**, 414-420 (2003).
8. D. A. McCormick, D. B. Nestvogel, B. J. He, Neuromodulation of Brain State and Behavior. *Annual Review of Neuroscience* **43**, null (2020).
9. B. van Vugt *et al.*, The threshold for conscious report: Signal loss and response bias in visual and frontal cortex. *Science* **360**, 537 (2018).
10. K. D. Harris, A. Thiele, Cortical state and attention. *Nature Reviews Neuroscience* **12**, 509-523 (2011).
11. M. S. Livingstone, D. H. Hubel, Effects of sleep and arousal on the processing of visual information in the cat. *Nature* **291**, 554-561 (1981).
12. D. A. McCormick, T. Bal, SLEEP AND AROUSAL: Thalamocortical Mechanisms. *Annual Review of Neuroscience* **20**, 185-215 (1997).
13. M. Vinck, R. Batista-Brito, U. Knoblich, J. A. Cardin, Arousal and locomotion make distinct contributions to cortical activity patterns and visual encoding. *Neuron* **86**, 740-754 (2015).
14. G. Aston-Jones, J. D. Cohen, An integrative theory of locus coeruleus-norepinephrine function: adaptive gain and optimal performance. *Annu Rev Neurosci* **28**, 403-450 (2005).
15. M. J. McGinley, S. V. David, D. A. McCormick, Cortical Membrane Potential Signature of Optimal States for Sensory Signal Detection. *Neuron* **87**, 179-192 (2015).
16. R. M. Yerkes, J. D. Dodson, The relation of strength of stimulus to rapidity of habit-formation. *Journal of Comparative Neurology and Psychology* **18**, 459-482 (1908).
17. M. A. Goodale, A. D. Milner, Separate visual pathways for perception and action. *Trends in Neurosciences* **15**, 20-25 (1992).
18. V. B. Mountcastle, The columnar organization of the neocortex. *Brain* **120 (Pt 4)**, 701-722 (1997).
19. Anna W. Roe *et al.*, Toward a Unified Theory of Visual Area V4. *Neuron* **74**, 12-29 (2012).
20. R. Desimone, J. Duncan, Neural mechanisms of selective visual attention. *Annu Rev Neurosci* **18**, 193-222 (1995).
21. C. J. McAdams, J. H. Maunsell, Effects of attention on orientation-tuning functions of single neurons in macaque cortical area V4. *The Journal of neuroscience : the official journal of the Society for Neuroscience* **19**, 431-441 (1999).
22. J. Moran, R. Desimone, Selective attention gates visual processing in the extrastriate cortex. *Science* **229**, 782-784 (1985).
23. J. H. Reynolds, T. Pasternak, R. Desimone, Attention increases sensitivity of V4 neurons. *Neuron* **26**, 703-714 (2000).
24. M. R. Cohen, J. H. Maunsell, Attention improves performance primarily by reducing interneuronal correlations. *Nat Neurosci* **12**, 1594-1600 (2009).
25. J. F. Mitchell, K. A. Sundberg, J. H. Reynolds, Differential attention-dependent response modulation across cell classes in macaque visual area V4. *Neuron* **55**, 131-141 (2007).
26. J. F. Mitchell, K. A. Sundberg, J. H. Reynolds, Spatial attention decorrelates intrinsic activity fluctuations in macaque area V4. *Neuron* **63**, 879-888 (2009).

27. S. Ghosh, J. H. R. Maunsell, Single trial neuronal activity dynamics of attentional intensity in monkey visual area V4. *Nature Communications* **12**, 2003 (2021).
28. A. Zénon, R. J. Krauzlis, Attention deficits without cortical neuronal deficits. *Nature* **489**, 434-437 (2012).
29. T. A. Engel *et al.*, Selective modulation of cortical state during spatial attention. *Science* **354**, 1140-1144 (2016).
30. J. van Kempen *et al.*, Top-down coordination of local cortical state during selective attention. *Neuron* **109**, 894-904.e898 (2021).
31. B. W. Connors, M. J. Gutnick, Intrinsic firing patterns of diverse neocortical neurons. *Trends Neurosci* **13**, 99-104 (1990).
32. H. Markram *et al.*, Interneurons of the neocortical inhibitory system. *Nature reviews. Neuroscience* **5**, 793-807 (2004).
33. M. Migliore, G. M. Shepherd, An integrated approach to classifying neuronal phenotypes. *Nature Reviews Neuroscience* **6**, 810-818 (2005).
34. C. P. Wonders, S. A. Anderson, The origin and specification of cortical interneurons. *Nature reviews. Neuroscience* **7**, 687-696 (2006).
35. H. Zeng, J. R. Sanes, Neuronal cell-type classification: challenges, opportunities and the path forward. *Nature Reviews Neuroscience* **18**, 530-546 (2017).
36. R. J. Douglas, K. A. C. Martin, NEURONAL CIRCUITS OF THE NEOCORTEX. *Annual Review of Neuroscience* **27**, 419-451 (2004).
37. R. J. Douglas, K. A. C. Martin, Mapping the Matrix: The Ways of Neocortex. *Neuron* **56**, 226-238 (2007).
38. J. A. Hirsch, L. M. Martinez, Laminar processing in the visual cortical column. *Curr Opin Neurobiol* **16**, 377-384 (2006).
39. A. S. Nandy, J. J. Nassi, J. H. Reynolds, Laminar Organization of Attentional Modulation in Macaque Visual Area V4. *Neuron* **93**, 235-246 (2017).
40. D. A. McCormick, B. W. Connors, J. W. Lighthall, D. A. Prince, Comparative electrophysiology of pyramidal and sparsely spiny stellate neurons of the neocortex. *J Neurophysiol* **54**, 782-806 (1985).
41. W. W. Pettine, N. A. Steinmetz, T. Moore, Laminar segregation of sensory coding and behavioral readout in macaque V4. *Proceedings of the National Academy of Sciences* **116**, 14749-14754 (2019).
42. A. D. Mehta, I. Ulbert, C. E. Schroeder, Intermodal selective attention in monkeys. I: distribution and timing of effects across visual areas. *Cerebral cortex (New York, N.Y. : 1991)* **10**, 343-358 (2000).
43. A. D. Mehta, I. Ulbert, C. E. Schroeder, Intermodal selective attention in monkeys. II: physiological mechanisms of modulation. *Cerebral cortex (New York, N.Y. : 1991)* **10**, 359-370 (2000).
44. E. A. Buffalo, P. Fries, R. Landman, T. J. Buschman, R. Desimone, Laminar differences in gamma and alpha coherence in the ventral stream. *Proc Natl Acad Sci U S A* **108**, 11262-11267 (2011).
45. D. Ferro, J. van Kempen, M. Boyd, S. Panzeri, A. Thiele, Directed information exchange between cortical layers in macaque V1 and V4 and its modulation by selective attention. *Proc Natl Acad Sci U S A* **118** (2021).

46. J. A. Westerberg, E. A. Sigworth, J. D. Schall, A. Maier, Pop-out search instigates beta-gated feature selectivity enhancement across V4 layers. *Proc Natl Acad Sci U S A* **118** (2021).
47. J. A. Westerberg, M. S. Schall, A. Maier, G. F. Woodman, J. D. Schall, Laminar microcircuitry of visual cortex producing attention-associated electric fields. *Elife* **11** (2022).
48. U. Mitzdorf, Current source-density method and application in cat cerebral cortex: investigation of evoked potentials and EEG phenomena. *Physiol Rev* **65**, 37-100 (1985).
49. Y. Kawaguchi, Groupings of nonpyramidal and pyramidal cells with specific physiological and morphological characteristics in rat frontal cortex. *Journal of Neurophysiology* **69**, 416-431 (1993).
50. L. G. Nowak, R. Azouz, M. V. Sanchez-Vives, C. M. Gray, D. A. McCormick, Electrophysiological classes of cat primary visual cortical neurons in vivo as revealed by quantitative analyses. *J Neurophysiol* **89**, 1541-1566 (2003).
51. J. Beatty, B. Lucero-Wagoner, The pupillary system. *Handbook of psychophysiology* **2** (2000).
52. E. H. Hess, J. M. Polt, Pupil size in relation to mental activity during simple problem-solving. *Science* **143**, 1190-1192 (1964).
53. J. Reimer *et al.*, Pupil Fluctuations Track Fast Switching of Cortical States during Quiet Wakefulness. *Neuron* **84**, 355-362 (2014).
54. L. Tang, M. J. Higley, Layer 5 Circuits in V1 Differentially Control Visuomotor Behavior. *Neuron* **105**, 346-354.e345 (2020).
55. R. J. Calin-Jageman, G. Cumming, Estimation for Better Inference in Neuroscience. *eneuro* **6**, ENEURO.0205-0219.2019 (2019).
56. J. Ho, T. Tumkaya, S. Aryal, H. Choi, A. Claridge-Chang, Moving beyond P values: data analysis with estimation graphics. *Nature Methods* **16**, 565-566 (2019).
57. R. Cools, M. D'Esposito, Inverted-U-shaped dopamine actions on human working memory and cognitive control. *Biol Psychiatry* **69**, e113-125 (2011).
58. P. R. Murphy, I. H. Robertson, J. H. Balsters, G. O'Connell R, Pupillometry and P3 index the locus coeruleus-noradrenergic arousal function in humans. *Psychophysiology* **48**, 1532-1543 (2011).
59. R. Rajagovindan, M. Ding, From prestimulus alpha oscillation to visual-evoked response: an inverted-U function and its attentional modulation. *J Cogn Neurosci* **23**, 1379-1394 (2011).
60. S. Vijayraghavan, M. Wang, S. G. Birnbaum, G. V. Williams, A. F. Arnsten, Inverted-U dopamine D1 receptor actions on prefrontal neurons engaged in working memory. *Nat Neurosci* **10**, 376-384 (2007).
61. P. W. Dicke, S. Chakraborty, P. Thier, Neuronal correlates of perceptual stability during eye movements. *European Journal of Neuroscience* **27**, 991-1002 (2008).
62. B. L. Zuber, L. Stark, Saccadic suppression: elevation of visual threshold associated with saccadic eye movements. *Exp Neurol* **16**, 65-79 (1966).
63. G. W. Beeler, Visual threshold changes resulting from spontaneous saccadic eye movements. *Vision Research* **7**, 769-775 (1967).

64. Z. M. Hafed, R. J. Krauzlis, Microsaccadic suppression of visual bursts in the primate superior colliculus. *The Journal of neuroscience : the official journal of the Society for Neuroscience* **30**, 9542-9547 (2010).
65. E. Lowet *et al.*, Enhanced Neural Processing by Covert Attention only during Microsaccades Directed toward the Attended Stimulus. *Neuron* **99**, 207-214.e203 (2018).
66. R. Engbert, R. Kliegl, Microsaccades uncover the orientation of covert attention. *Vision Research* **43**, 1035-1045 (2003).
67. Z. M. Hafed, J. J. Clark, Microsaccades as an overt measure of covert attention shifts. *Vision Research* **42**, 2533-2545 (2002).
68. E. Gowen, R. V. Abadi, E. Poliakoff, P. C. Hansen, R. C. Miall, Modulation of saccadic intrusions by exogenous and endogenous attention. *Brain Res* **1141**, 154-167 (2007).
69. G. Galfano, E. Betta, M. Turatto, Inhibition of return in microsaccades. *Experimental brain research* **159**, 400-404 (2004).
70. A. Pastukhov, J. Braun, Rare but precious: microsaccades are highly informative about attentional allocation. *Vision Res* **50**, 1173-1184 (2010).
71. G. Yu, J. P. Herman, L. N. Katz, R. J. Krauzlis, Microsaccades as a marker not a cause for attention-related modulation. *Elife* **11** (2022).
72. N. A. Steinmetz, T. Moore, Eye movement preparation modulates neuronal responses in area V4 when dissociated from attentional demands. *Neuron* **83**, 496-506 (2014).
73. P. Fries, Neuronal Gamma-Band Synchronization as a Fundamental Process in Cortical Computation. *Annual Review of Neuroscience* **32**, 209-224 (2009).
74. P. Fries, T. Womelsdorf, R. Oostenveld, R. Desimone, The effects of visual stimulation and selective visual attention on rhythmic neuronal synchronization in macaque area V4. *The Journal of neuroscience : the official journal of the Society for Neuroscience* **28**, 4823-4835 (2008).
75. A. G. Siapas, E. V. Lubenov, M. A. Wilson, Prefrontal Phase Locking to Hippocampal Theta Oscillations. *Neuron* **46**, 141-151 (2005).
76. M. Vinck, M. van Wingerden, T. Womelsdorf, P. Fries, C. M. Pennartz, The pairwise phase consistency: a bias-free measure of rhythmic neuronal synchronization. *NeuroImage* **51**, 112-122 (2010).
77. P. Mitra, *Observed brain dynamics* (Oxford University Press, 2007).
78. J. D. Semedo *et al.*, Feedforward and feedback interactions between visual cortical areas use different population activity patterns. *Nat Commun* **13**, 1099 (2022).
79. P. P. Mitra, B. Pesaran, Analysis of dynamic brain imaging data. *Biophys J* **76**, 691-708 (1999).
80. Z. W. Davis, L. Muller, J. Martinez-Trujillo, T. Sejnowski, J. H. Reynolds, Spontaneous travelling cortical waves gate perception in behaving primates. *Nature* **587**, 432-436 (2020).
81. T. Moore, M. Zirnsak, Neural Mechanisms of Selective Visual Attention. *Annual Review of Psychology* **68**, 47-72 (2017).
82. R. J. Schafer, T. Moore, Selective attention from voluntary control of neurons in prefrontal cortex. *Science* **332**, 1568-1571 (2011).

83. T. Moore, M. Fallah, Control of eye movements and spatial attention. *Proc Natl Acad Sci U S A* **98**, 1273-1276 (2001).
84. S. Martinez-Conde, J. Otero-Millan, S. L. Macknik, The impact of microsaccades on vision: towards a unified theory of saccadic function. *Nature Reviews Neuroscience* **14**, 83-96 (2013).
85. H. Spitzer, R. Desimone, J. Moran, Increased attention enhances both behavioral and neuronal performance. *Science* **240**, 338-340 (1988).
86. R. Moreno-Bote *et al.*, Information-limiting correlations. *Nat Neurosci* **17**, 1410-1417 (2014).
87. D. Contreras, L. Palmer, Response to contrast of electrophysiologically defined cell classes in primary visual cortex. *The Journal of neuroscience : the official journal of the Society for Neuroscience* **23**, 6936-6945 (2003).
88. R. C. Foehring, N. M. Lorenzon, P. Herron, C. J. Wilson, Correlation of physiologically and morphologically identified neuronal types in human association cortex in vitro. *J Neurophysiol* **66**, 1825-1837 (1991).
89. N. V. Povysheva *et al.*, Properties of excitatory synaptic responses in fast-spiking interneurons and pyramidal cells from monkey and rat prefrontal cortex. *Cerebral cortex (New York, N.Y. : 1991)* **16**, 541-552 (2006).
90. A. Hasenstaub *et al.*, Inhibitory postsynaptic potentials carry synchronized frequency information in active cortical networks. *Neuron* **47**, 423-435 (2005).
91. A. Schurger, F. Pereira, A. Treisman, J. D. Cohen, Reproducibility distinguishes conscious from nonconscious neural representations. *Science* **327**, 97-99 (2010).
92. A. I. Abbas *et al.*, Somatostatin Interneurons Facilitate Hippocampal-Prefrontal Synchrony and Prefrontal Spatial Encoding. *Neuron* **100**, 926-939.e923 (2018).
93. P. Fries, J. H. Reynolds, A. E. Rorie, R. Desimone, Modulation of Oscillatory Neuronal Synchronization by Selective Visual Attention. *Science* **291**, 1560 (2001).
94. G. Rohenkohl, C. A. Bosman, P. Fries, Gamma Synchronization between V1 and V4 Improves Behavioral Performance. *Neuron* **100**, 953-963.e953 (2018).
95. M. S. Worden, J. J. Foxe, N. Wang, G. V. Simpson, Anticipatory biasing of visuospatial attention indexed by retinotopically specific alpha-band electroencephalography increases over occipital cortex. *The Journal of neuroscience : the official journal of the Society for Neuroscience* **20**, Rc63 (2000).
96. J. H. Marshel *et al.*, Cortical layer–specific critical dynamics triggering perception. *Science* **365**, eaaw5202 (2019).
97. M. Steriade, A. Nuñez, F. Amzica, A novel slow (< 1 Hz) oscillation of neocortical neurons in vivo: depolarizing and hyperpolarizing components. *The Journal of neuroscience : the official journal of the Society for Neuroscience* **13**, 3252-3265 (1993).
98. M. von Krosigk, T. Bal, D. McCormick, Cellular mechanisms of a synchronized oscillation in the thalamus. *Science* **261**, 361-364 (1993).
99. E. Zohary, M. N. Shadlen, W. T. Newsome, Correlated neuronal discharge rate and its implications for psychophysical performance. *Nature* **370**, 140-143 (1994).
100. S. Dehaene, J.-P. Changeux, Experimental and Theoretical Approaches to Conscious Processing. *Neuron* **70**, 200-227 (2011).

101. J. J. Nassi, M. C. Avery, A. H. Cetin, A. W. Roe, J. H. Reynolds, Optogenetic Activation of Normalization in Alert Macaque Visual Cortex. *Neuron* **86**, 1504-1517 (2015).
102. O. Ruiz *et al.*, Optogenetics through windows on the brain in the nonhuman primate. *J Neurophysiol* **110**, 1455-1467 (2013).
103. J. A. Hartigan, P. M. Hartigan, The dip test of unimodality. *The annals of Statistics*, 70-84 (1985).
104. D. H. McDougal, P. D. Gamlin, Autonomic control of the eye. *Compr Physiol* **5**, 439-473 (2015).
105. H. Hoffmann (2015) violin.m - Simple violin plot using matlab default kernel density estimation. (, INRES (University of Bonn), Katzenburgweg 5, 53115 Germany.).
106. S. D. König, E. A. Buffalo, A nonparametric method for detecting fixations and saccades using cluster analysis: removing the need for arbitrary thresholds. *Journal of neuroscience methods* **227**, 121-131 (2014).
107. B. Efrom, R. J. Tibshirani, An introduction to the bootstrap. *Champman and Hall/CRC* (1993).
108. H. Hotelling, "Relations Between Two Sets of Variates" in Breakthroughs in Statistics: Methodology and Distribution, S. Kotz, N. L. Johnson, Eds. (Springer New York, New York, NY, 1992), 10.1007/978-1-4612-4380-9_14, pp. 162-190.

Figure 1

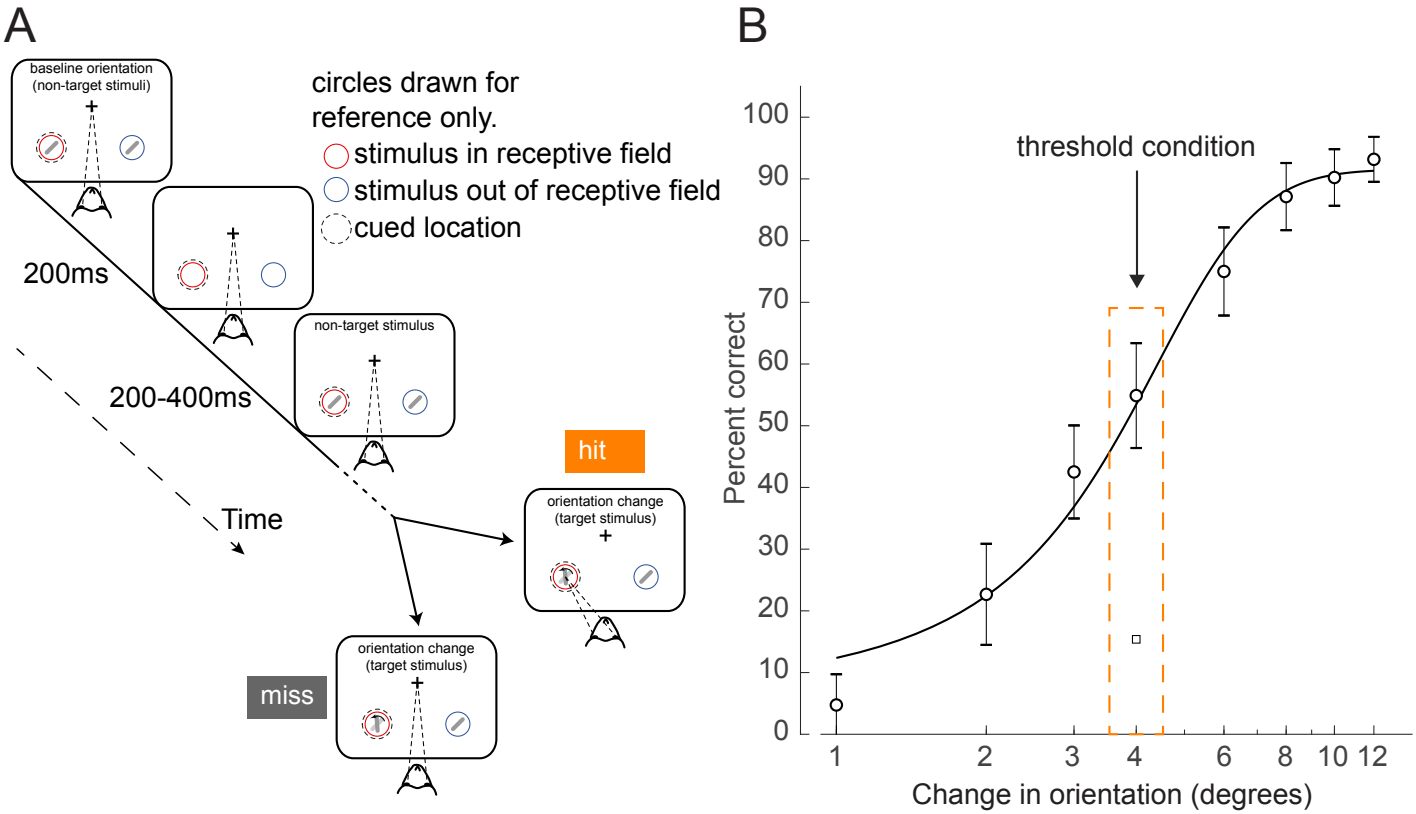

Figure 1. Orientation change detection task at perceptual threshold
(**A**) Schematic of task structure. The monkey initiated a trial by fixating on the center of the screen. Two Gabor stimuli (represented by oriented lines) were presented for 200 ms and then turned off for 200-400ms. This was repeated until, at an unpredictable time, one of the stimuli changed orientation. The monkey could report having seen the change by making an eye movement to the location of the target stimulus to receive a reward (hit trials). If the monkey failed to report the orientation change and maintained fixation on the center of the screen it was not rewarded (miss trials). Before a block of trials, the monkey was cued as to which stimulus was likely to undergo the change (95% valid cue). In 5% of trials the orientation change occurred at the other location (foil trials). Circles indicating the cued location and receptive field are drawn for figure reference only and were not presented during the task. (**B**) Example behavioral psychometric function from one recording session and attention condition. Behavioral performance (hit rate, circles) is presented as a function of orientation change. Data was fitted with a logistic function. The threshold condition, trials with performance halfway between the upper and lower asymptotes of the logistic function, is indicated by the orange box. Error bars represent standard deviation calculated with a jackknife procedure (20 jackknives). The square symbol indicates foil trial performance.

Figure 2

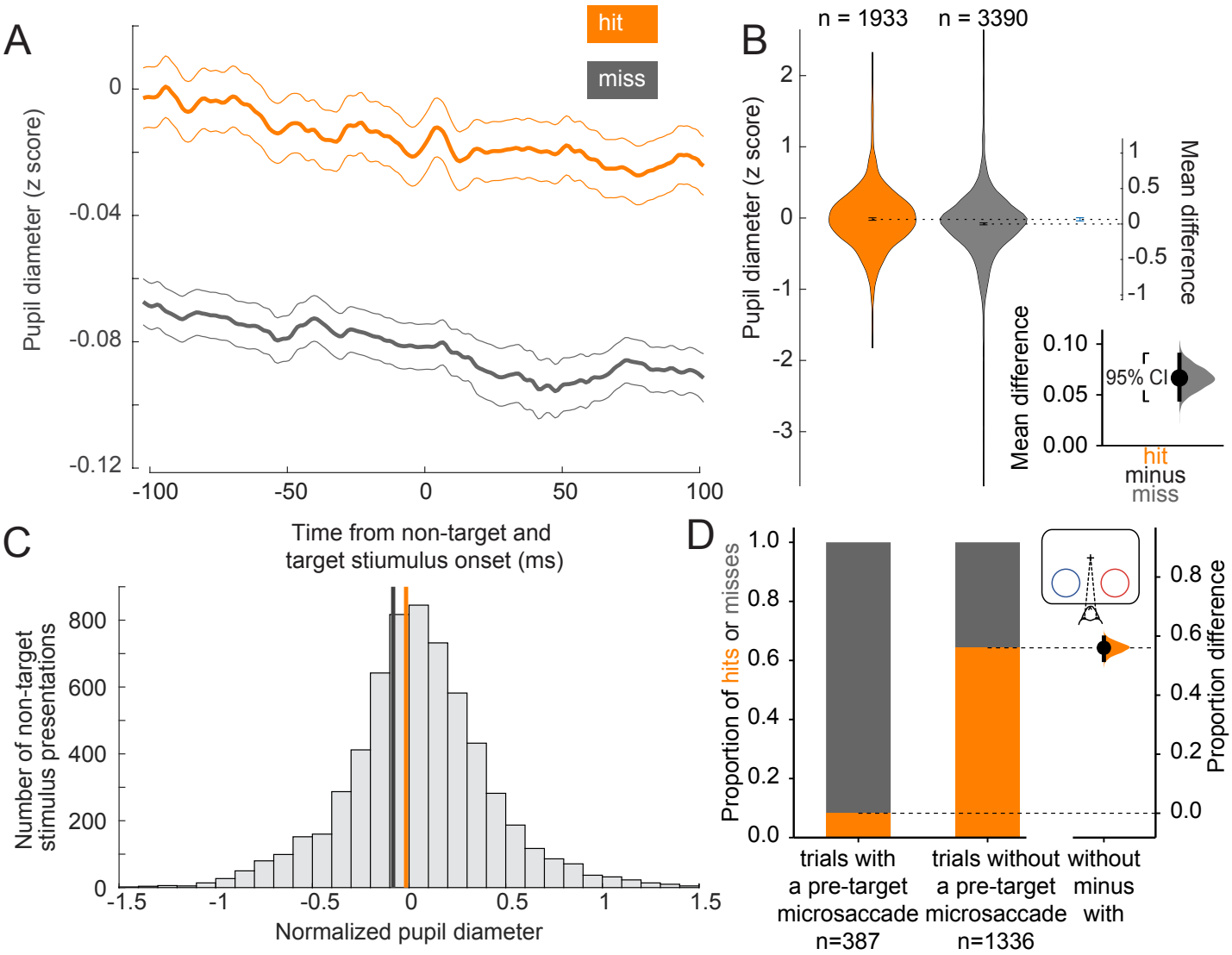

Figure 2. Hit trials have larger pupil diameter whereas microsaccades more often precede misses
(**A**) Normalized pupil diameter for hit and miss trials in the threshold condition. 0 ms corresponds to non-target and target stimulus onset. Mean +/- s.e.m. (**B**) Distribution of pupil diameter values associated with hit and miss trials. Pupil diameter was averaged from 100ms before to 100ms after non-target and target stimulus onset. Violin plots were generated using kernel smoothing (See Methods). Error bars represent 95% confidence intervals for the mean of each distribution, and the mean difference (blue, right axes). Inset: zoomed in view of the mean difference between hit and miss trials. Black bar represents a 95% confidence interval of the mean difference. Shaded region reflects the distribution of the bootstrapped estimation of the mean difference. (**C**) Histogram of mean pupil diameter around the time of non-target and target stimulus onset (calculated as in **B**). Orange and gray lines represent the mean pupil diameter for hit and miss trials respectively. (**D**) Left: Hit rate for trials with (387 trials) and without (right, 1336 trials) a microsaccade detected in the time window 0-400ms before target onset. Right: Bootstrapped estimation of the mean difference in hit proportion in trials with vs without a pre-target microsaccade. Same conventions as **2B**.

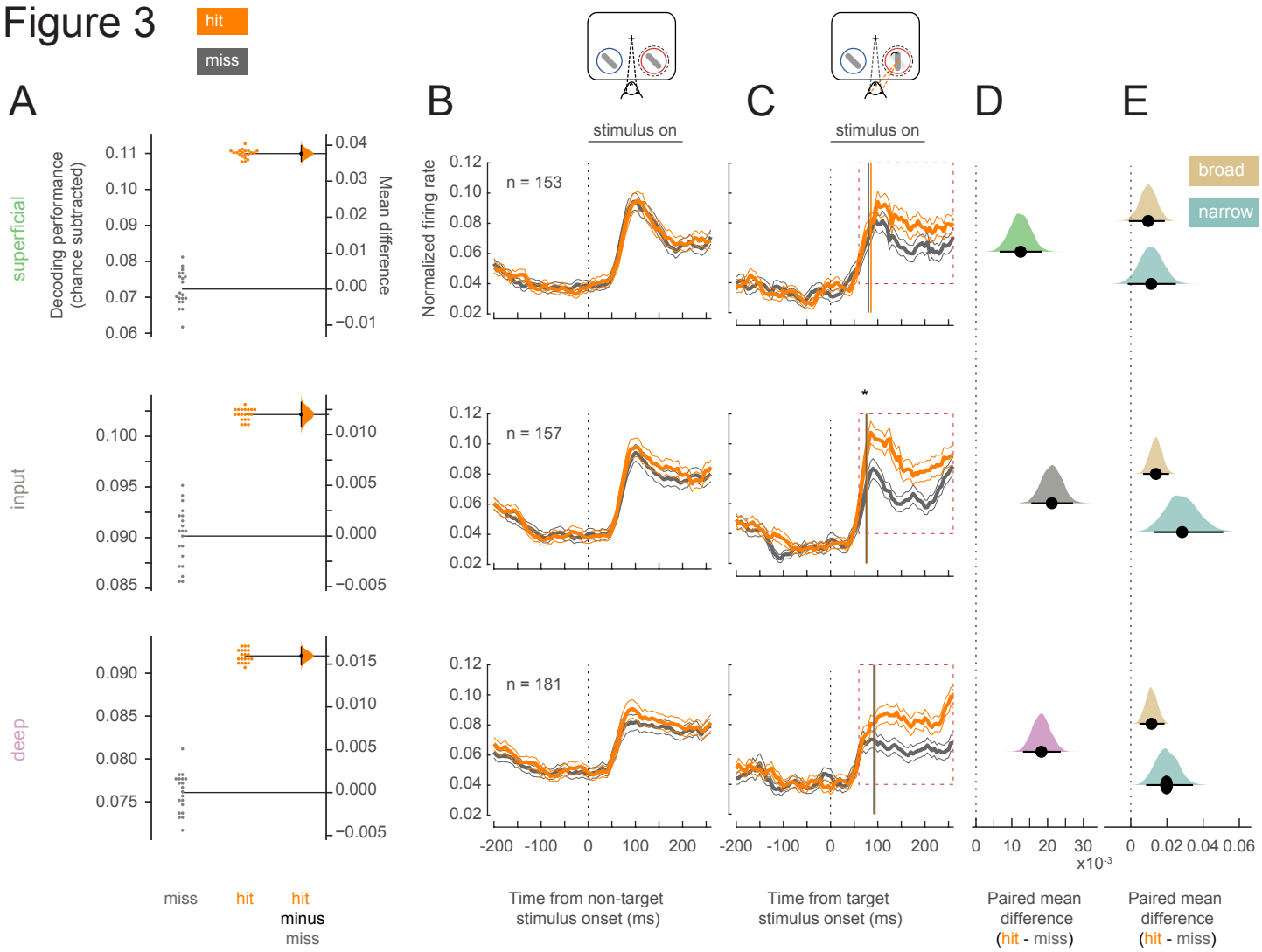

Figure 3. Target stimuli evoke higher firing rates in hit trials
Rows correspond to different layers (top=superficial, middle=input, bottom=deep). (**A**) Performance for decoding targets from non-targets from single-units and multi-units in each layer. Points in the left section of each plot show the decoding performance for each of the 20 different cross-validations. The right section for each layer shows the bootstrapped estimation of the difference between decoding performance between hits and misses. Half-violin plots show the bootstrapped distribution of the difference, and black dots and bars represent the mean and 95% confidence intervals of the difference in decoding performance. Chance levels, determined by shuffling target and non-target identity, were subtracted from the raw decoding performance values. (**B**) Non-target population (single and multi-unit) PSTH of visually responsive neurons for the hit (orange) and miss (dark-gray) trials in the threshold condition (mean +/- s.e.m). The horizontal black bar indicates the time and duration of stimulus presentation. (**C**) As in **B** but for target stimuli. The star indicates the time at which firing rates in the input layer first differ significantly between hit and miss trials. Vertical lines represent the mean time at which firing rates for each neuron rise above the 95% confidence interval of their baseline activity (see also Figure S3C). (**D**) Bootstrapped estimation of the paired mean difference in target stimulus-evoked firing rate between hit and miss trials in the time window 60-260ms (red dotted box in **C**) after target stimulus onset. Shaded regions represent the bootstrapped estimation of the paired mean difference in firing rate (hit - miss), and black lines are 95% confidence intervals. Plots include data from both single and multi-units, separated by layer (top= superficial, middle=input, bottom=deep). (**E**) As in **D**, bootstrapped estimation of the paired mean difference in firing rate for hit trials compared to miss trials in the target stimulus-evoked period, but only for single-units broken up by cell class (gold=broad, teal=narrow).

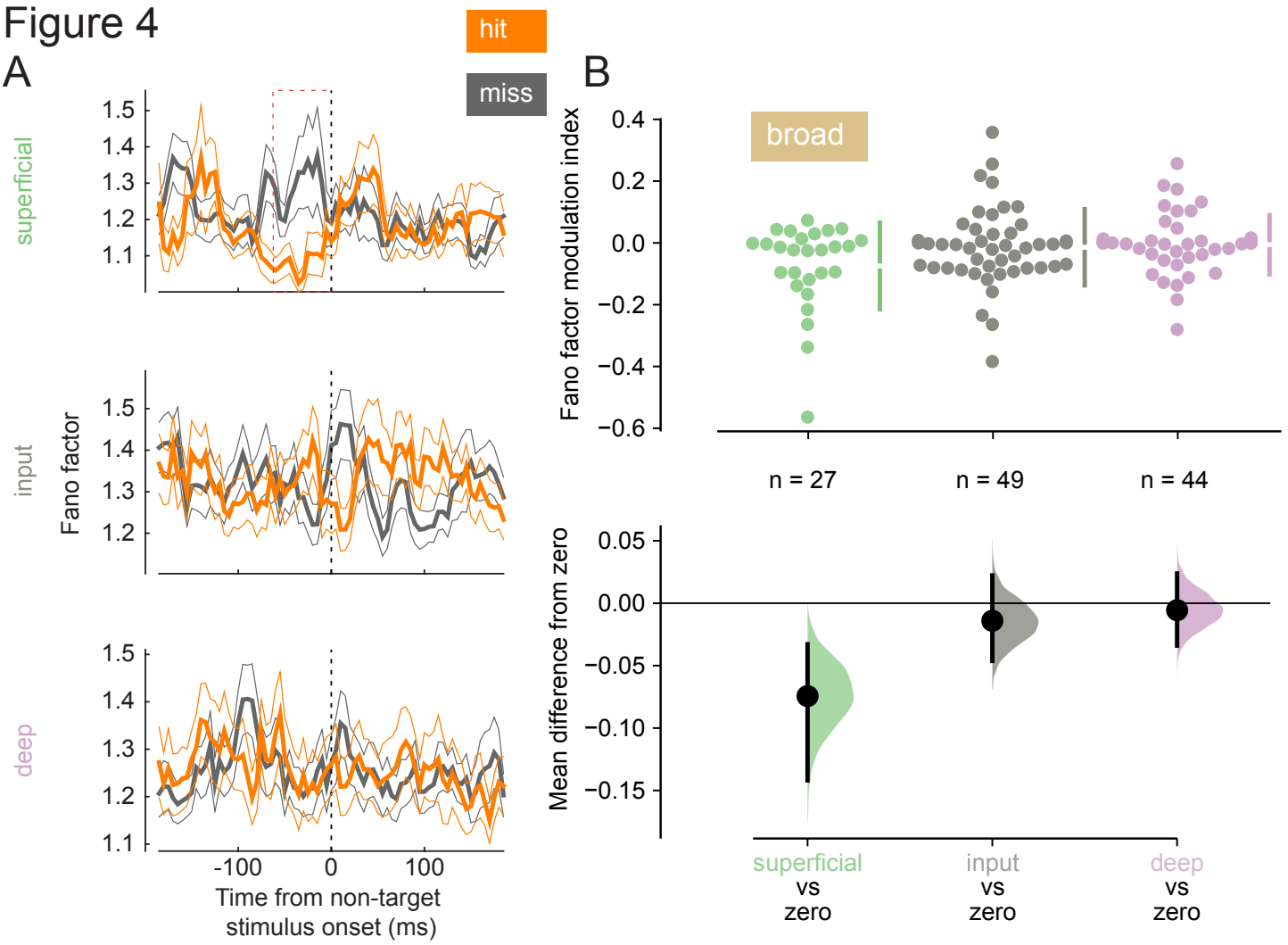

Figure 4. Broad-spiking neurons in the superficial layer have decreased variability in hit trials
(**A**) Rows correspond to different layers (top=superficial, middle=input, bottom=deep). The Fano factor of broad-spiking putative excitatory neurons for the hit and miss trials in the threshold condition (mean +/- s.e.m). There is a significant decrease in variability for the hit trials prior to stimulus onset only in the superficial layer. 0 ms corresponds to non-target stimulus onset. The average Fano factor within a 60ms time-window (red dashed box) prior to non-target stimulus onset is plotted in **B**. (**B**) Top: Fano factor modulation index for each broad-spiking neurons recorded in each layer, averaged in the 60ms preceding non-target stimulus onset. Bottom: Bootstrapped estimation of the mean difference of the Fano factor modulation index from zero in each of the three layers. Colored curves represent the estimated bootstrapped distribution. Black dots and lines reflect the mean and 95% confidence intervals of the distributions.

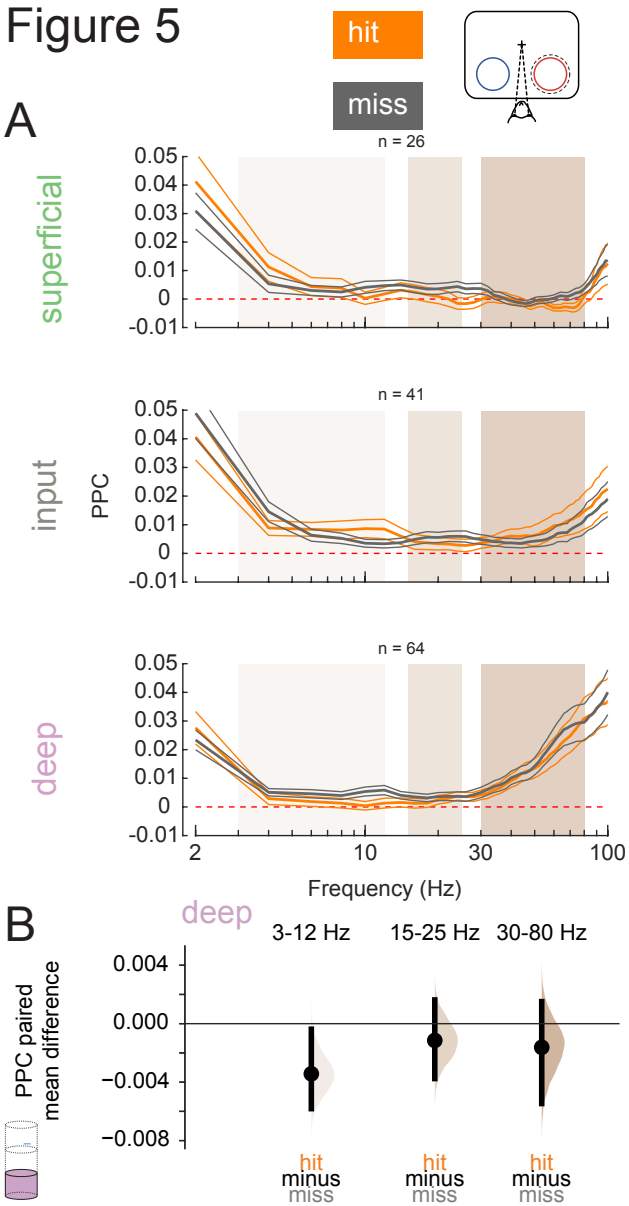

Figure 5. Deep layer neurons are phase-locked to low-frequency rhythms in miss trials
(**A**) Pairwise phase consistency (PPC) of single and multi-units in each layer to the local field potential (LFP) signal recorded from the same channel in hit and miss trials at threshold. PPC was calculated in the pre-stimulus period (0-200 ms before stimulus onset). Dashed red line indicates a PPC of 0, below which there is no consistent relationship between spikes and LFP phase. (**B**) Bootstrapped estimation plot for the paired mean difference in PPC for deep layer neurons over three frequency bands: 3-12Hz, 15-25Hz, 30-80Hz. Curves represent the bootstrapped distribution for the paired difference, and black dots and vertical lines represent the mean and 95% confidence intervals for the paired mean difference.

Figure 6

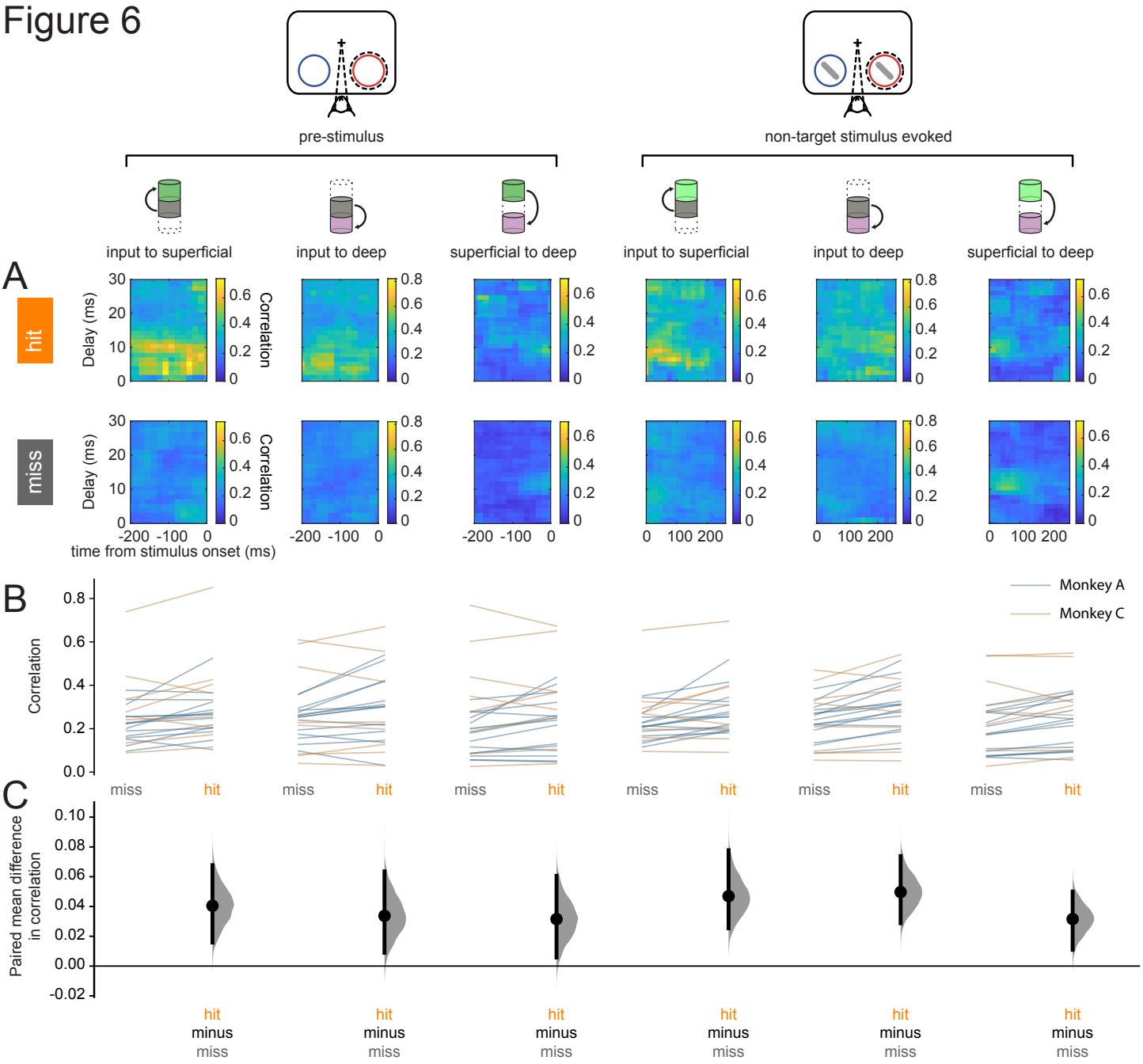

Figure 6. Hit trials are characterized by stronger feed-forward interlaminar population correlations
(**A**) CCA-based population correlation as a function of time and inter-laminar delay during the pre-stimulus and stimulus-evoked periods in hit and miss trials in an example session. (**B**) Mean feed-forward population correlation in each session. Color indicates the monkey (blue=monkey A, yellow=monkey C). (**C**) Bootstrapped estimation plot for the paired mean difference in population correlation for each pair of layers and time window (pre-stimulus or stimulus-evoked). Curves represent the bootstrapped distribution for the paired difference, and black dots and vertical lines represent the mean and 95% confidence intervals for the paired mean difference.

Figure 7

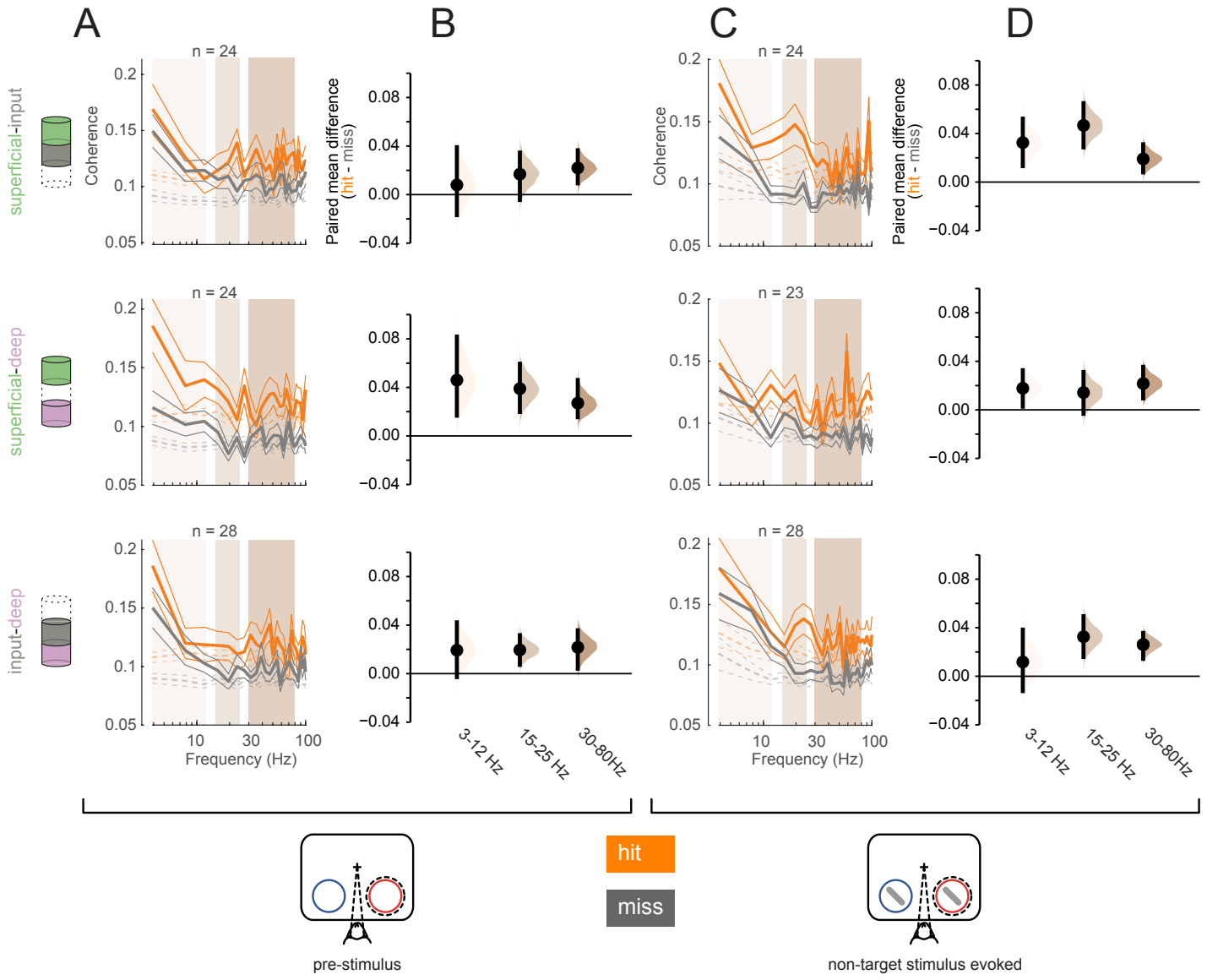

Figure 7. Greater interlaminar coherence in hit trials in the pre-stimulus and non-target stimulus-evoked periods Rows correspond to different pairs of layers (top=superficial-input, middle=superficial-deep, bottom=input-deep). (**A**) Multi-unit interlaminar spike-spike coherence (SSC) calculated in the 200ms before non-target stimulus onset in hit and miss trials (solid lines, mean +/- s.e.m). Firing rates were matched across hit and miss trials. Dashed lines represent coherence calculated with shuffled trial identities (mean +/- s.e.m). (**B**) Bootstrapped estimation plot for the paired mean difference in SSC for each pair of layers averaged over three frequency bands : 3-12Hz, 15-25Hz, 30-80Hz. Curves represent the bootstrapped distribution for the paired difference, and black dots and vertical lines represent the mean and 95% confidence intervals for the paired mean difference. (**C**) Interlaminar spike-spike coherence in the non-target stimulus-evoked period (60-260ms after stimulus onset). Same conventions as in **A**. (**D**) Bootstrapped estimation plot for the paired mean difference in SSC for each pair of layers averaged over three frequency bands. Same conventions as **B**.

Figure 8

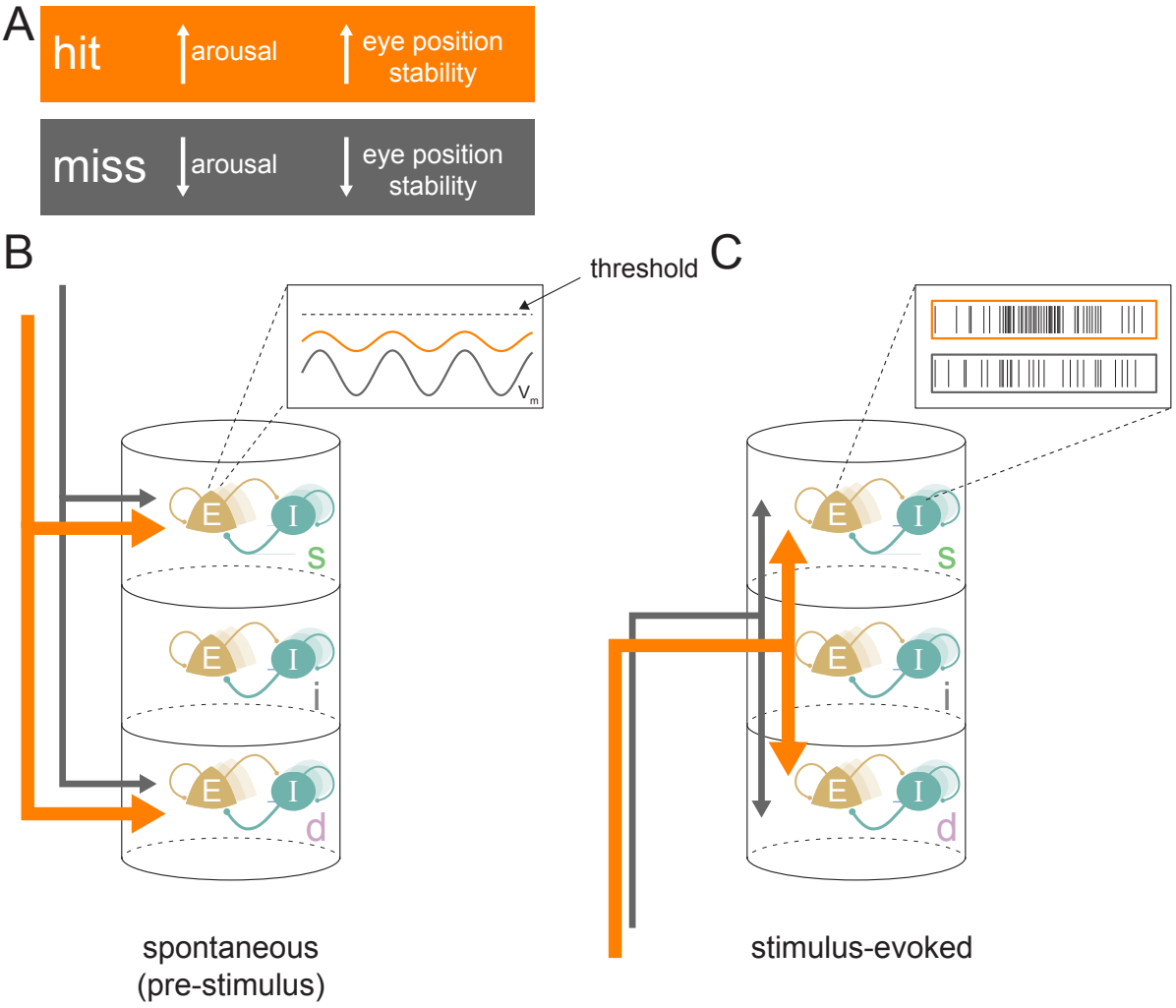

Figure 8. Conceptual model for stimulus processing at perceptual threshold
(**A**) Hit trials have a larger pupil diameter and fewer pre-target microsaccades, reflecting a state of increased arousal and greater eye position stability. Conversely, miss trials show decreased arousal and eye position stability. (**B**) In the spontaneous pre-stimulus period, hits are characterized by decreased variability in superficial layer broad-spiking neurons, which we hypothesize is reflective of lower membrane potential (Vm) variability (inset). Hit trials are also characterized by greater synchrony between the superficial and deep layers (indicated by thicker arrows), which could be reflecting a stronger top-down influence on the cortical column. (**C**) In the stimulus-evoked period there is greater interlaminar synchrony between pairs that include the input layer (represented by thicker arrows), which we propose reflects improved feed-forward propagation of information. We propose these state differences in hits contribute to elevated firing rates in response to target stimuli, particularly in the superficial layers (inset), resulting in a higher-fidelity output to downstream areas. E = excitatory; I = inhibitory; s = superficial; i = input; d = deep.

Figure 1-figure supplement 1

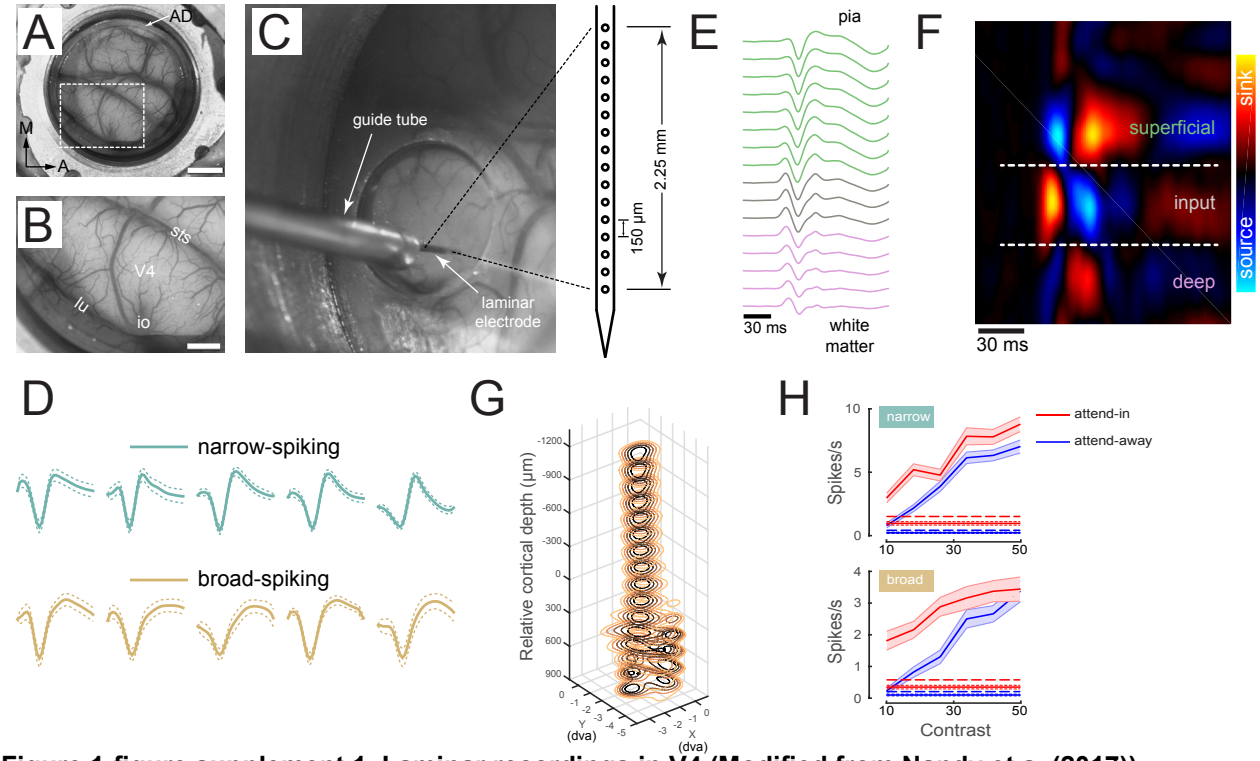

Figure 1-figure supplement 1. Laminar recordings in V4 (Modified from Nandy et a. (2017)).
(**A**) An artificial dura (AD) chamber is shown over dorsal V4 in the right hemisphere of Monkey A. The native dura mater was resected and replaced with a silicone based artificial dura, thereby providing an optically clear window into the cortex. Scale bar = 5mm. (**B**) An enlarged view of the boxed region in **A** clearly shows the sulci and the microvasculature. sts = superior temporal sulcus, lu = lunate sulcus, io = inferior occipital sulcus. Area V4 lies on the pre-lunate gyrus between the superior temporal and lunate sulci. Scale bar = 2mm. (**C**) Electrophysiology setup: a plastic stabilizer with a circular aperture is secured in place inside the chamber such that the aperture is centered over the pre-lunate gryus. A 16-channel linear array electrode (electrode spacing 150 µm) is positioned over the center of the gyrus and lowered into the cortex under microscopic guidance. The microvasculature pattern was used as a reference to target different cortical sites across recording sessions. (**D**) Example recording session in monkey C depicting 12 single unit waveforms (mean +/- s.e.m.) isolated along the cortical column. Teal waveforms correspond to narrow-spiking putative interneurons and gold waveforms correspond to broad-spiking putative excitatory units. (**E**) Stimulus triggered local field potentials (LFPs) obtained by flashing 30ms high contrast ring stimuli in the receptive field of a V4 cortical column. LFP traces averaged across all stimulus repeats are shown color-coded as being part of either the superficial (green), input (gray) or deep (pink) layers. Layer assignment was done after current source-density analysis. (**F**) Current source-density (CSD) calculated as the second spatial derivative of the stimulus triggered LFPs and displayed as a colored map. The x-axis represents time from stimulus onset; the y-axis represents cortical depth oriented such that the pial surface is at the top and the white matter is at the bottom. Red hues represent current sink, blue hues represent current source. The input layer is identified as the first current sink followed by a reversal to current source. The superficial and deep layers have the opposite sink-source pattern. The CSD map has been spatially smoothed for visualization. (**G**) Stacked contour plots show spatial receptive fields (RFs) mapped along each contact point in the laminar probe. The spatial receptive fields were obtained by applying reverse correlation to the LFP power evoked by sparse pseudo-random sequences of Gabor stimuli. The RFs are well aligned, indicating perpendicular penetration down a cortical column. Zero depth represents the center of the input layer as estimated from the CSD. (**H**) Contrast response functions – spikes rate as a function of stimulus contrast – are shown for 2 example units identified in a single recording session in Monkey A. Red and blue traces correspond to the attend-in to RF and attend-away from RF conditions respectively. The dotted lines represent the corresponding background firing-rates. The dashed lines are 4 standard deviations above baseline. A unit was considered as visually responsive, if the contrast response functions exceeded this threshold in both the attention conditions. Mean +/- s.e.m. Panels are reproduced from Nandy et al. (2017).

Figure 1-figure supplement 2

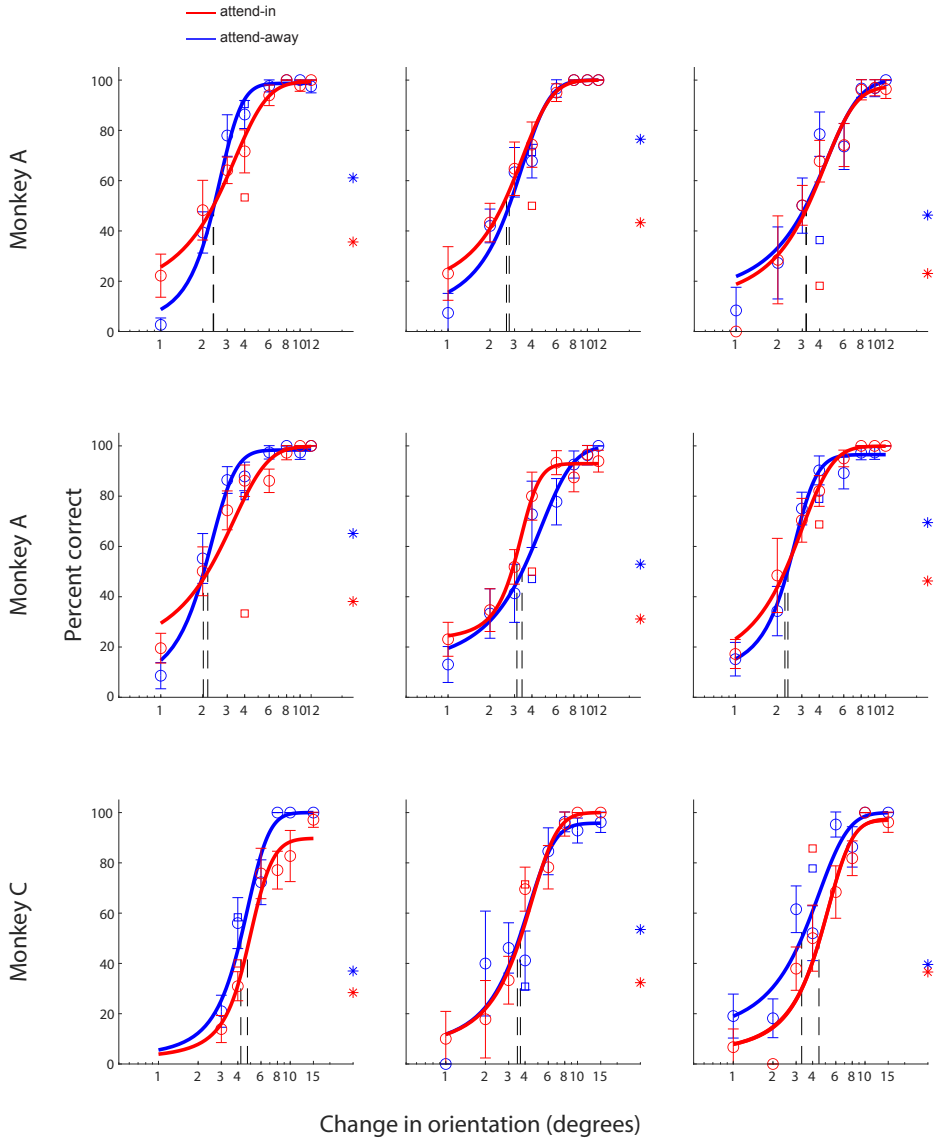

Figure 1-figure supplement 2. Additional psychometric function examples.
Example behavioral psychometric functions from 9 recording sessions in the attend in (red) and attend away (blue) conditions. Behavioral performance (circles) is presented as a function of orientation change. Data was fitted with a logistic function. The threshold of each fitted logistic function is indicated by the vertical dashed line. The square symbol indicates foil trial performance, and the star symbol indicates catch trial performance.

Figure 1-figure supplement 3

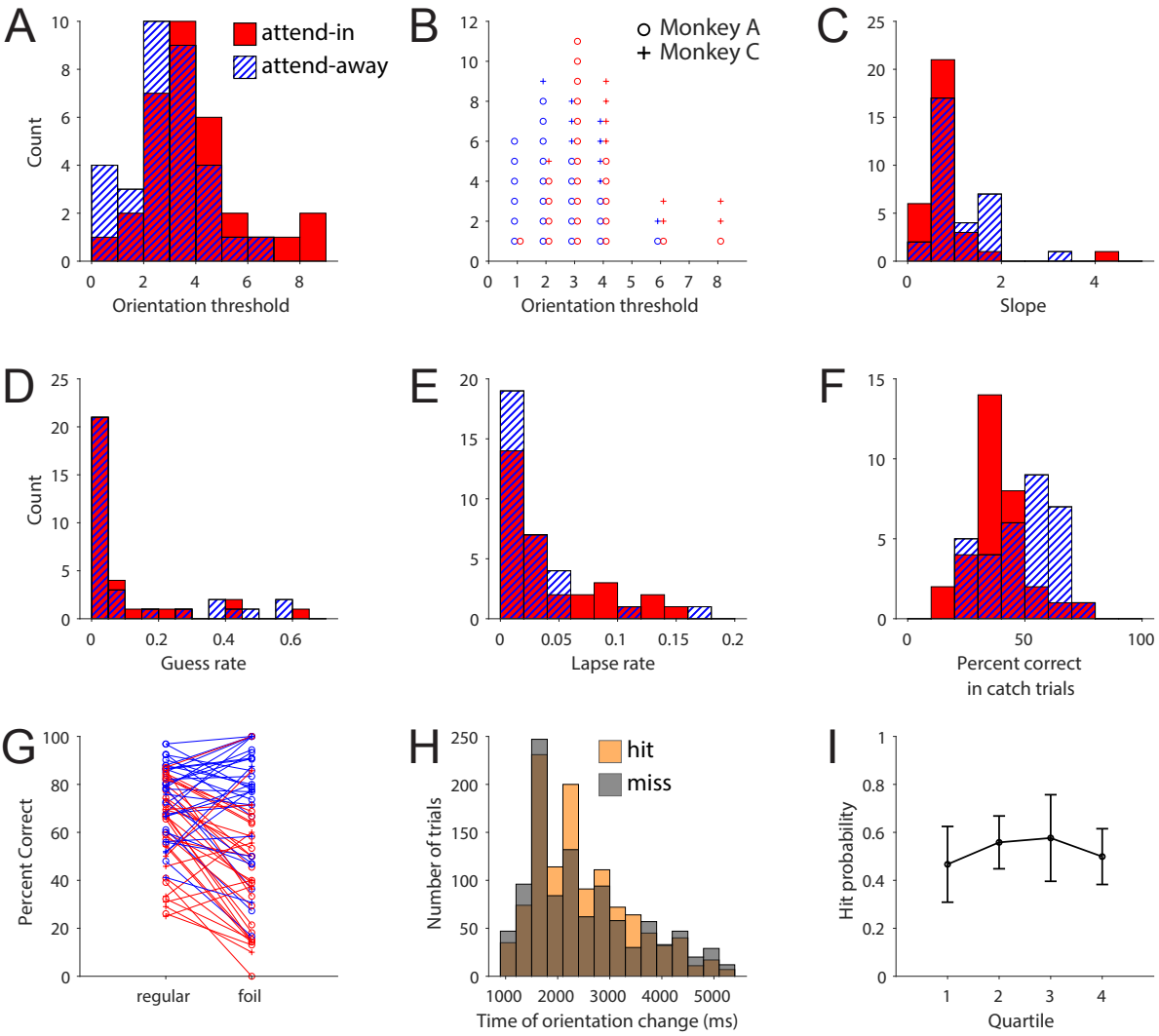

Figure 1-figure supplement 3. Psychometric function parameters.
(**A**) Distribution of the orientation threshold of the fitted psychometric functions in the attend-in (red solid) and attend-away (blue hatch) conditions for each recording session. The threshold of the sigmoid may not correspond exactly to an orientation change tested in the experiment. (**B**) Distribution of threshold orientation changes used as the threshold condition in the rest of this study (red=attend-in, blue=attend-away, circle=monkey A, plus=monkey C). (**C**) Distribution of slopes for the fitted psychometric functions (same conventions as **A**). (**D**) Distribution of guess rate for the fitted psychometric functions (same conventions as **A**). (**E**) Distribution of lapse rate for the fitted psychometric functions (same conventions as **A**). (**F**) Distribution of catch trial performance in each session (same conventions as **A**). (**G**) Performance on orientation-change matched regular trials (target presented at cued location) and foil trials (target presented at uncued location) for each session (same conventions as **B**). (**H**) Distribution of target presentation time for hit (orange) and miss (gray) trials. (**I**) Performance in threshold trials in each recording session split by quartiles (see Methods). Error bars represent standard deviation.

Figure 2-figure supplement 1

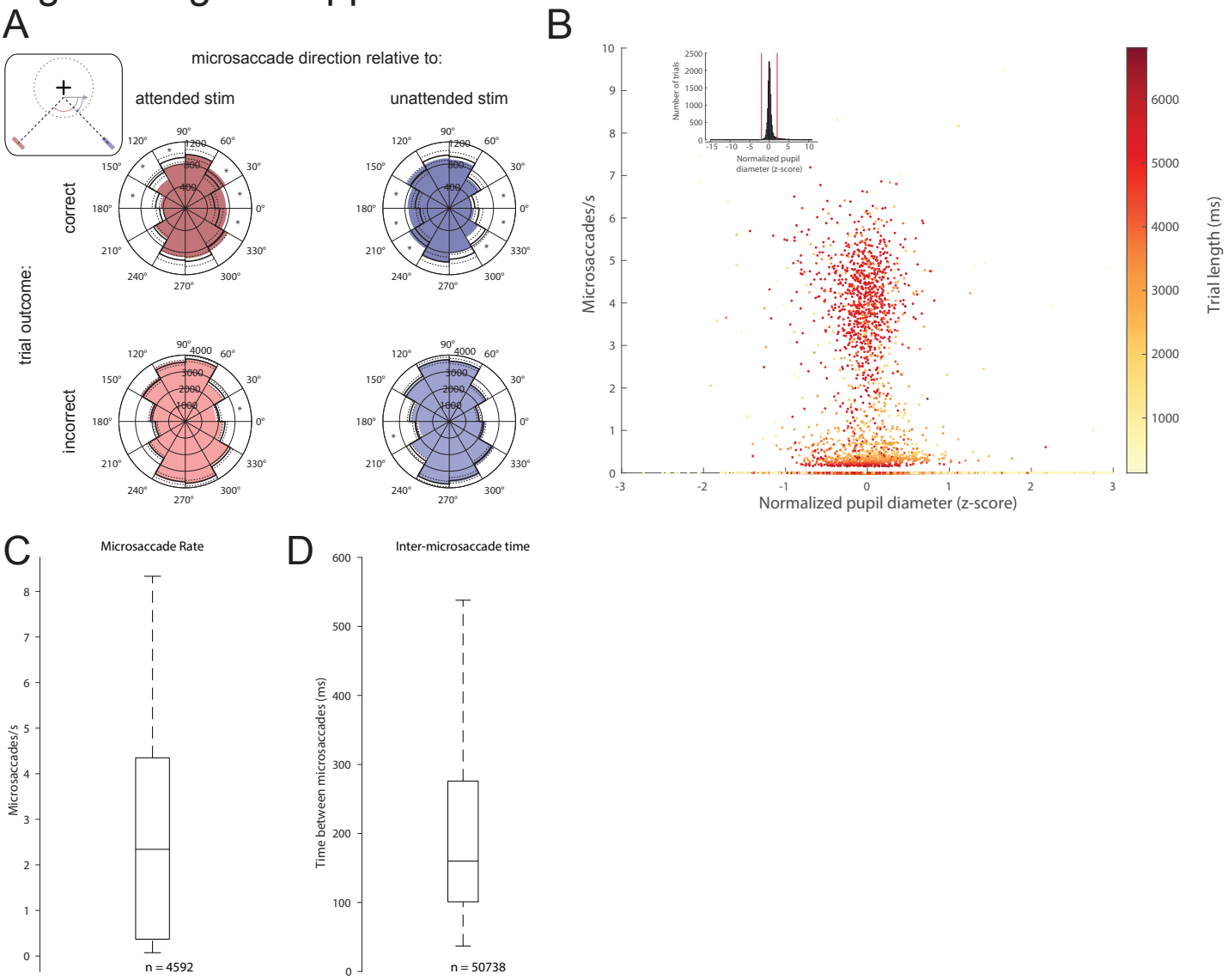

Figure 2-figure supplement 1. Microsaccades are preferentially directed towards the target in correct trials and have a slight correlation with pupil diameter

Data is presented for all trials, regardless of orientation change (not just the threshold condition). (**A**) The histograms represent the direction of microsaccades relative to the attended stimulus (left column) or unattended stimulus (right column) in correct (top row) and incorrect (bottom row) trials. Black lines represent the mean (solid) and 99.5% confidence interval (dashed) of the bootstrapped null distribution estimated by pooling correct and incorrect microsaccades. *p < 0.005. Inset: Schematic for calculation of relative microsaccade direction. Microsaccade is represented by the gray arrow (**B**) Scatterplot of microsaccade rate versus mean normalized pupil diameter, shows a small but statistically significant relationship between the two quantities (r2 = 0.006, p<0.001). Each dot is color-coded by trial length. Inset: Histogram of mean pupil diameter for all trials, including those less than -2 or greater than 2 (red lines). Only four of the trials with pupil diameters less than -2 or greater than 2 had detected microsaccades. (**C**) Boxplot of microsaccade rates for all trials. (**D**) Boxplot of the time between microsaccades recorded in the same trial. 4% of microsaccades separated by more than 538ms were excluded as outliers (See Methods).

Figure 2-figure supplement 2

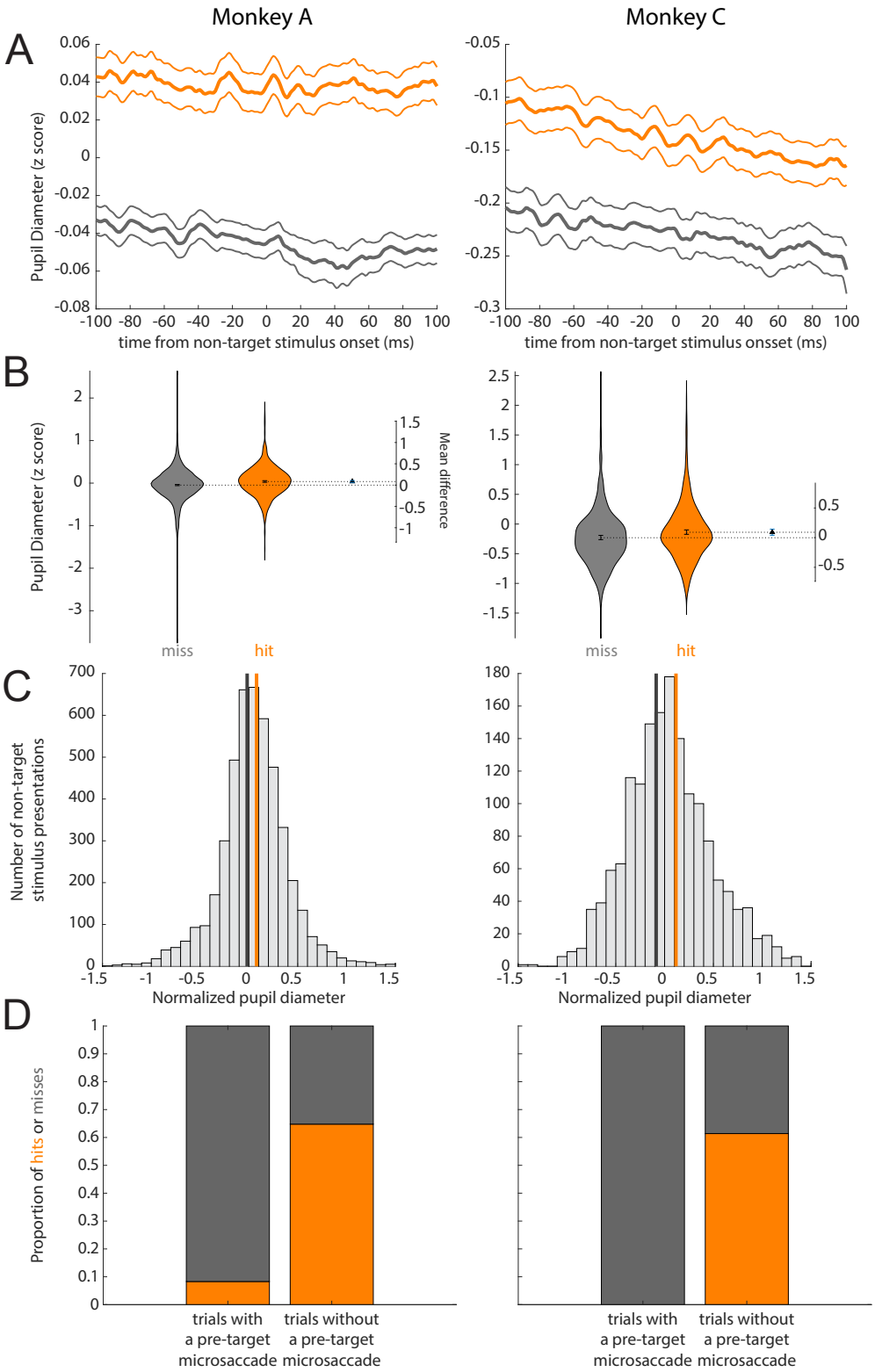

Figure 2-figure supplement 2. Single monkey pupil diameter and microsaccade data. (**A**) Normalized pupil diameter for hit and miss trails in the threshold condition separated by monkey. 0 ms corresponds to non-target and target stimulus onset. Mean +/- s.e.m. (**B**) Distribution of pupil diameter values associated with hit and miss trials separated by monkey. Pupil diameter was averaged from 100ms before to 100ms after non-target and target stimulus onset. Violin plots were generated using kernel smoothing (See Methods). Error bars represent 95% confidence intervals for the mean of each distribution, and the mean difference (blue, right axes). (**C**) Histogram of mean pupil diameter around the time of non-target and target stimulus onset for each monkey (calculated as in **B**). Orange and gray lines represent the mean pupil diameter for hit and miss trials respectively. (**D**) Hit rate for trials with and without a microsaccade detected in the time window 0-400ms before target onset for each monkey.

Figure 3-figure supplement 1

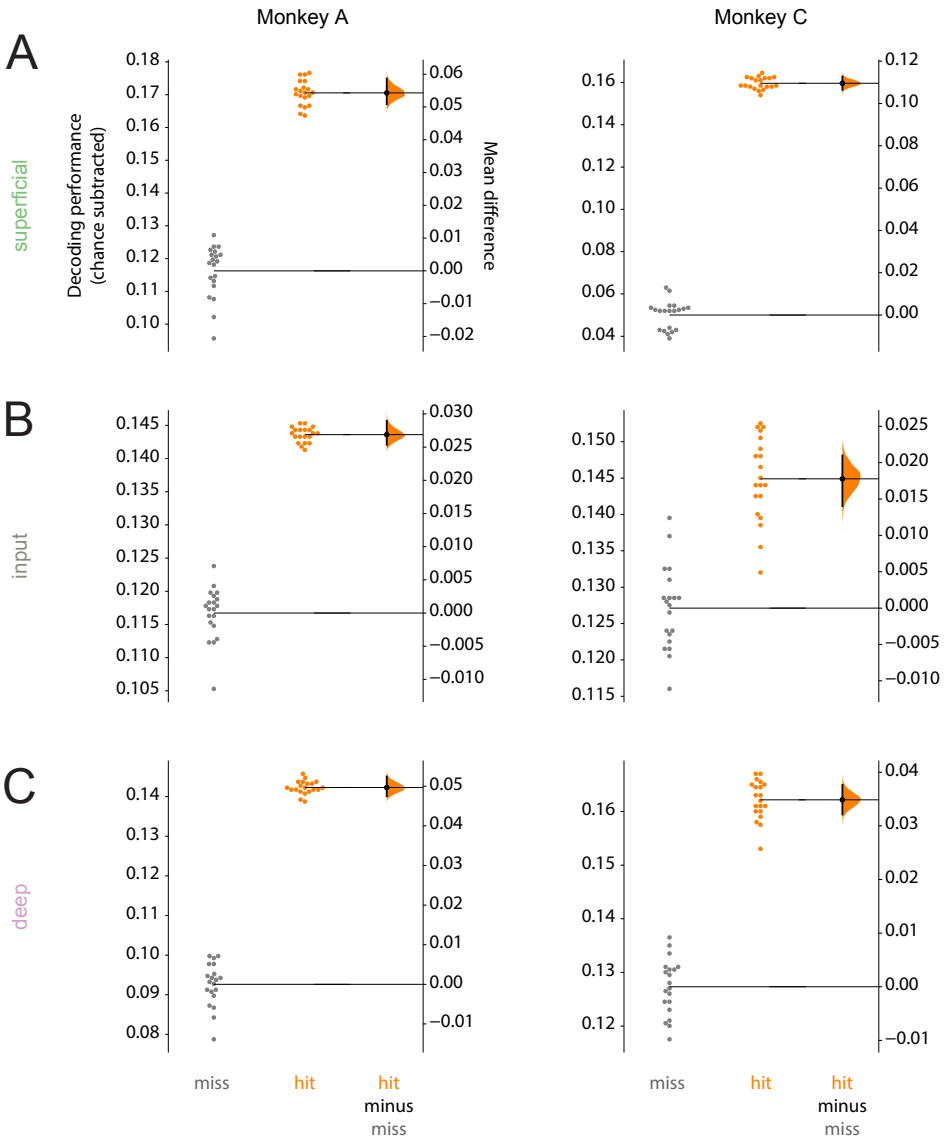

Figure 3-figure supplement 1. Single monkey decoding performance
(**A**) Performance for decoding targets from non-targets from single-units and multi-units in the superficial layer for individual monkeys. Points in the left section of each plot show the decoding performance for each of the 20 different cross-validations. The right section for each layer shows the bootstrapped estimation of the difference between decoding performance in hits and misses. Half-violin plots show the bootstrapped distribution of the difference, and black dots and bars represent the mean and 95% confidence intervals of the difference in decoding performance. Chance levels, determined by shuffling target and non-target identity, were subtracted from the raw decoding performance values. (**B**) Same as **A** but for the input layer. (**C**) Same as **A** but for the deep layers.

Figure 3-figure supplement 2

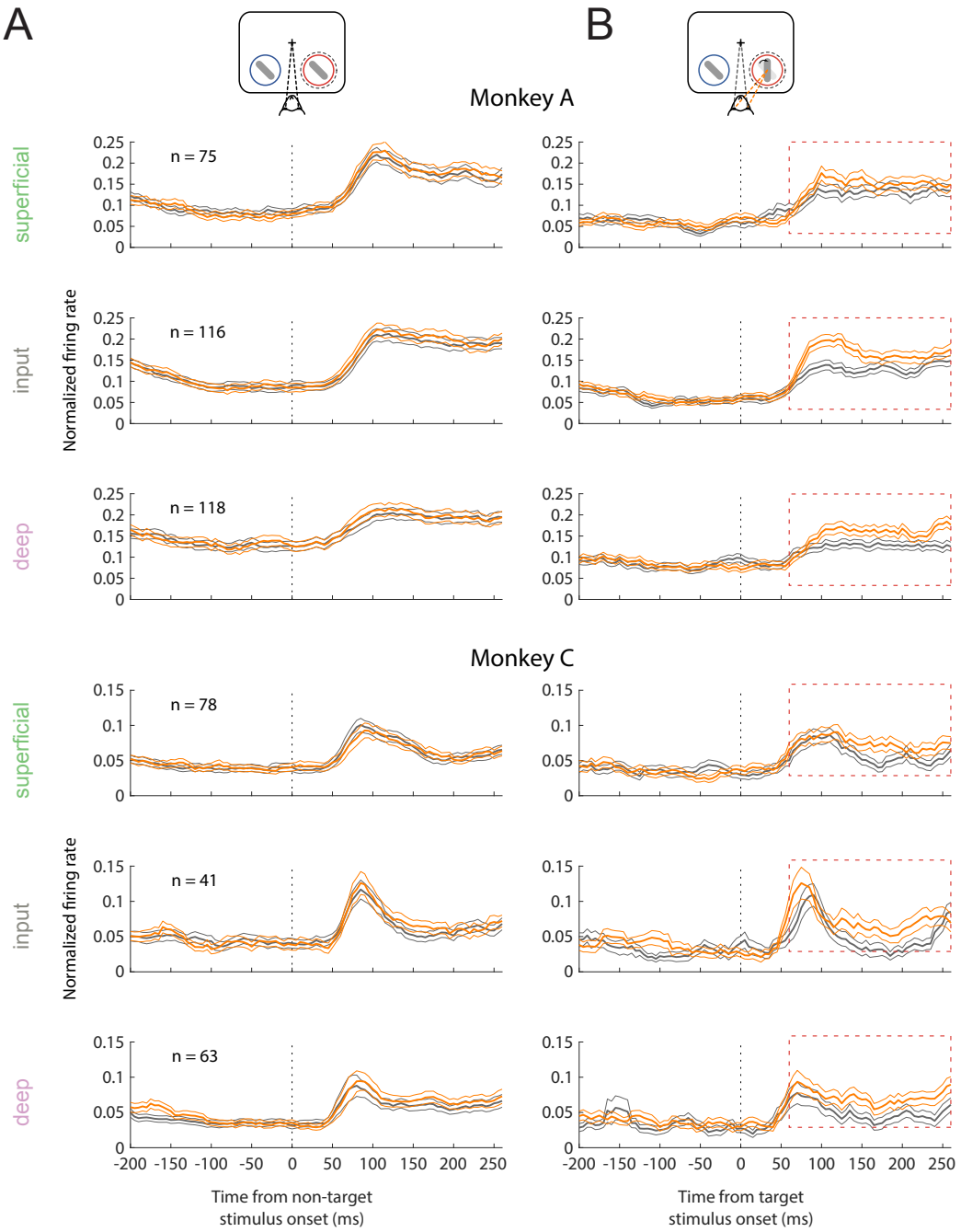

Figure 3-figure supplement 2. Single monkey firing rate data
(**A**) Single monkey non-target population (single and multi-unit) PSTH of visually responsive neurons for the hit (orange) and miss (dark-gray) trials in the threshold condition (mean +/- s.e.m). (**B**) As in **A** but for target stimuli. Red box indicates the time window used for analysis in **3C**.

Figure 3-figure supplement 3

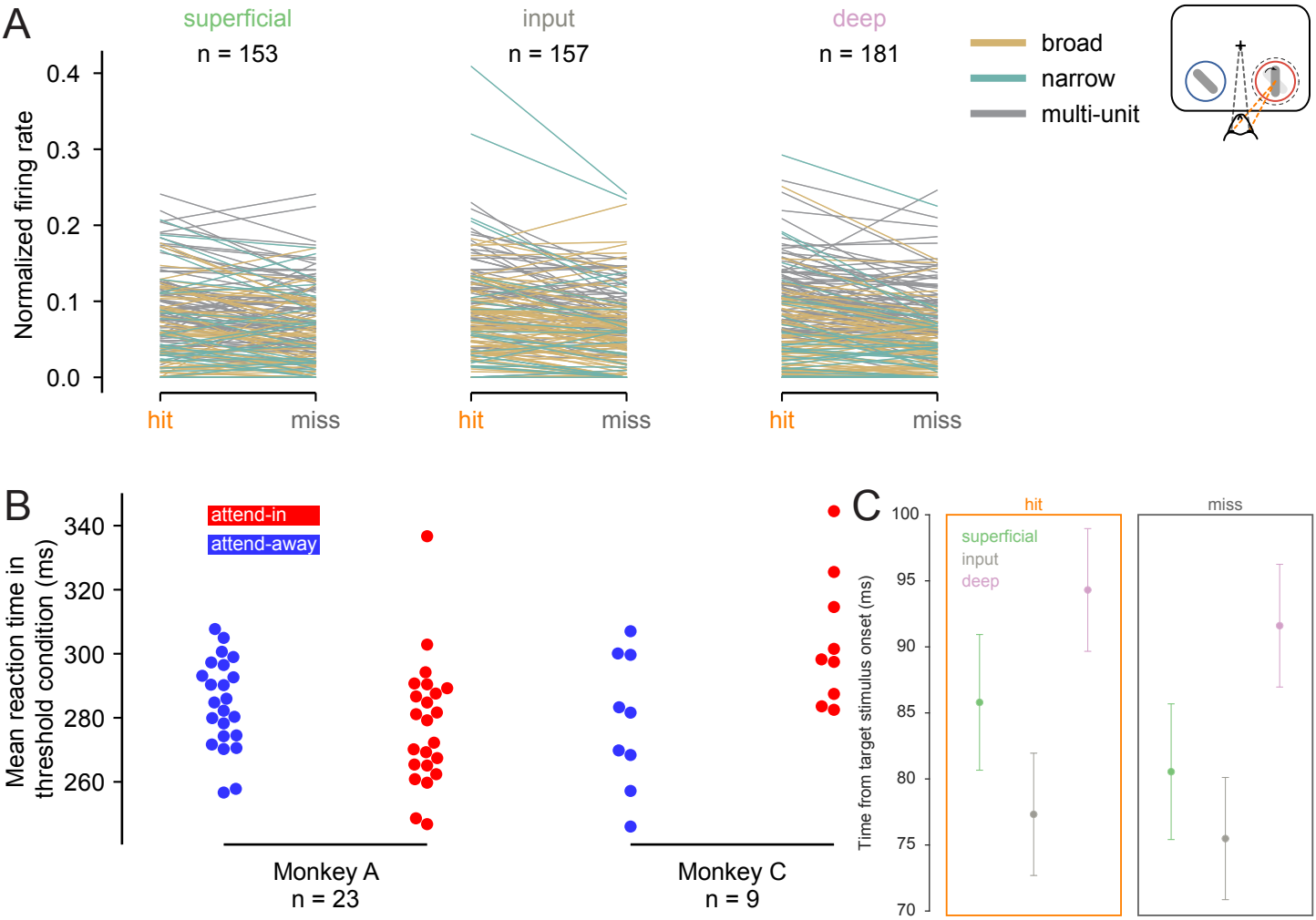

Figure 3-figure supplement 3. Firing rates for individual neurons and reaction time in threshold condition
(**A**) Target stimulus-evoked normalized firing rates in hit and miss trials for each recorded single and multi-unit cluster in hit and miss trials. Clusters are divided by layer: left=superficial, middle=input, right=deep. Related to **Figure 3B**. Each line represents the mean firing rate in response to target stimuli in hit and miss trials for a given unit. Data is color coded by unit type (gold=broad, teal=narrow, gray=multi-unit). See Methods for normalization method. (**B**) Mean reaction time (time from target stimulus onset to saccade onset) for hit trials in the threshold condition in both attend-in (red) and attend-away (blue) trials for each recording session. (**C**) Mean time at which single- and multi-unit firing rates rise significantly above pre-stimulus baseline in response to target stimuli in hit and miss trials. Mean +/- s.e.m.

Figure 4-figure supplement 1

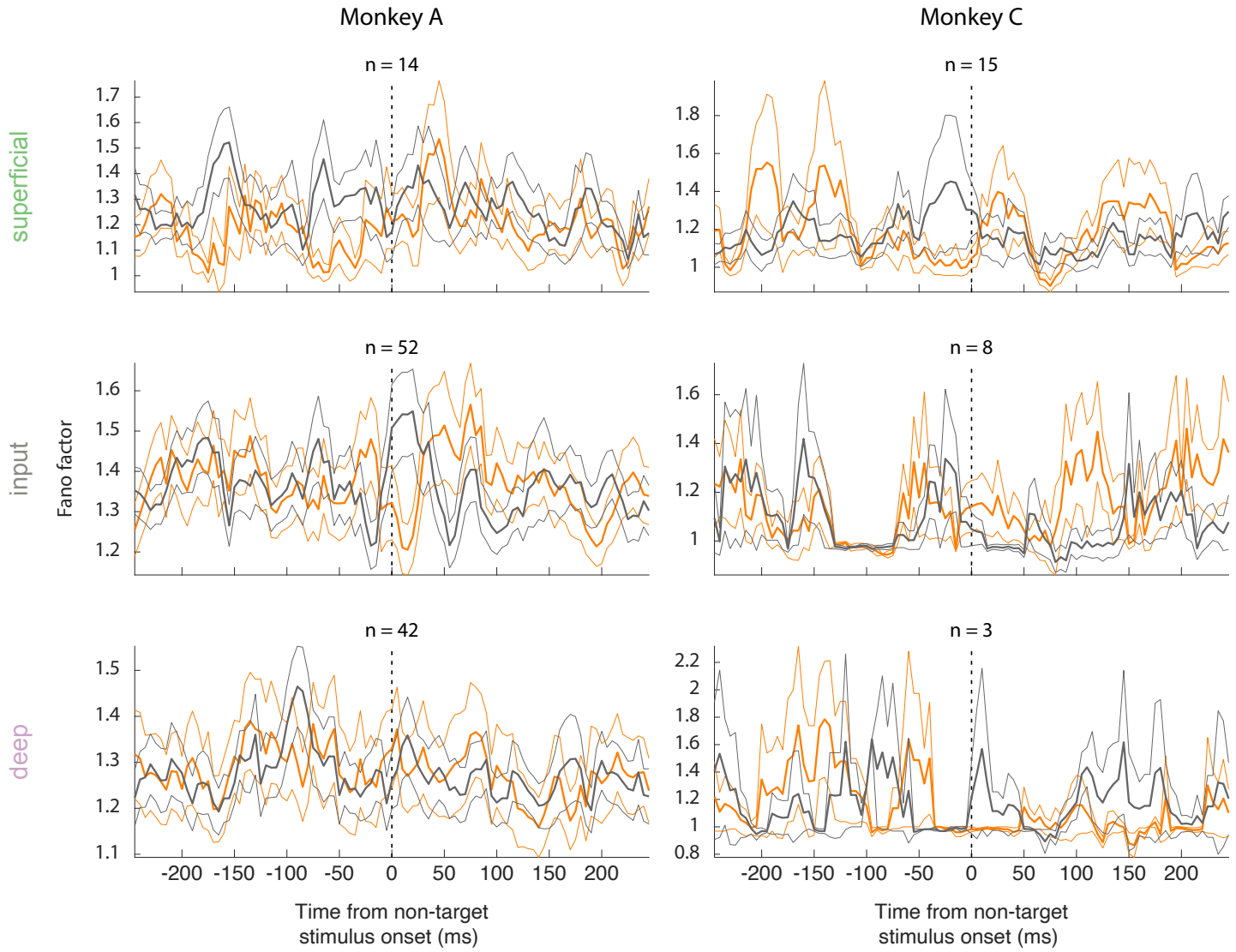

Figure 4-figure supplement 1. Single monkey Fano factor data
Rows correspond to different layers (top=superficial, middle=input, bottom=deep) and columns correspond to monkeys. The Fano factor of broad-spiking putative excitatory neurons for the hit and miss trials in the threshold condition in each monkey (mean +/- s.e.m).

Figure 4-figure supplement 2

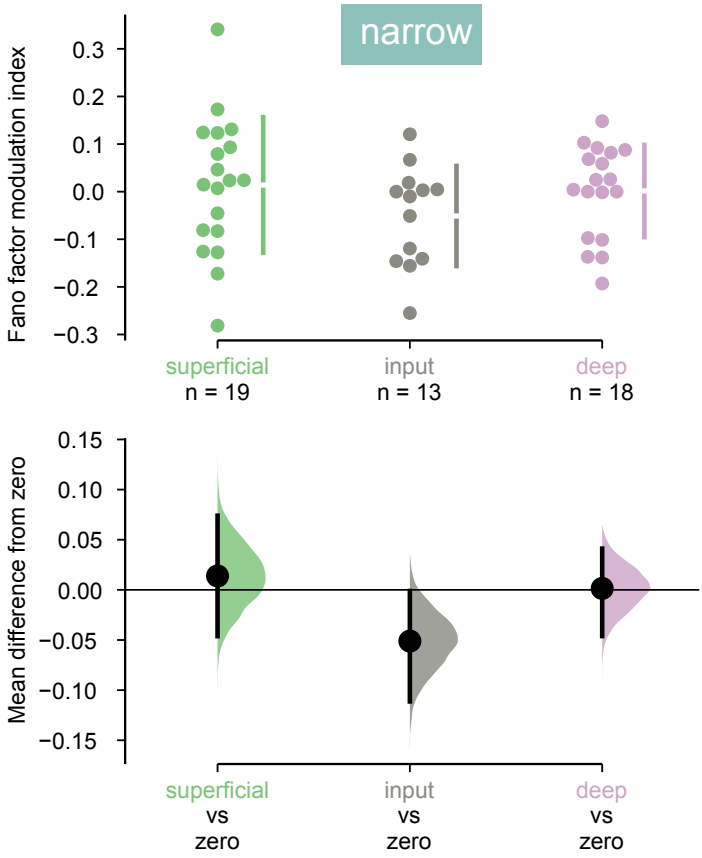

Figure 4-figure supplement 2. Narrow-spiking neurons do not have decreased variability in hit trials
Top: Fano factor modulation index for each narrow-spiking neurons recorded in each layer, averaged in the 60ms preceding non-target stimulus onset. Bottom: Bootstrapped estimation of the mean difference of the Fano factor modulation index from zero in each of the three layers. Colored curves represent the estimated bootstrapped distribution. Black dots and lines reflect the mean and 95% confidence intervals of the distributions.

Figure 5-figure supplement 1

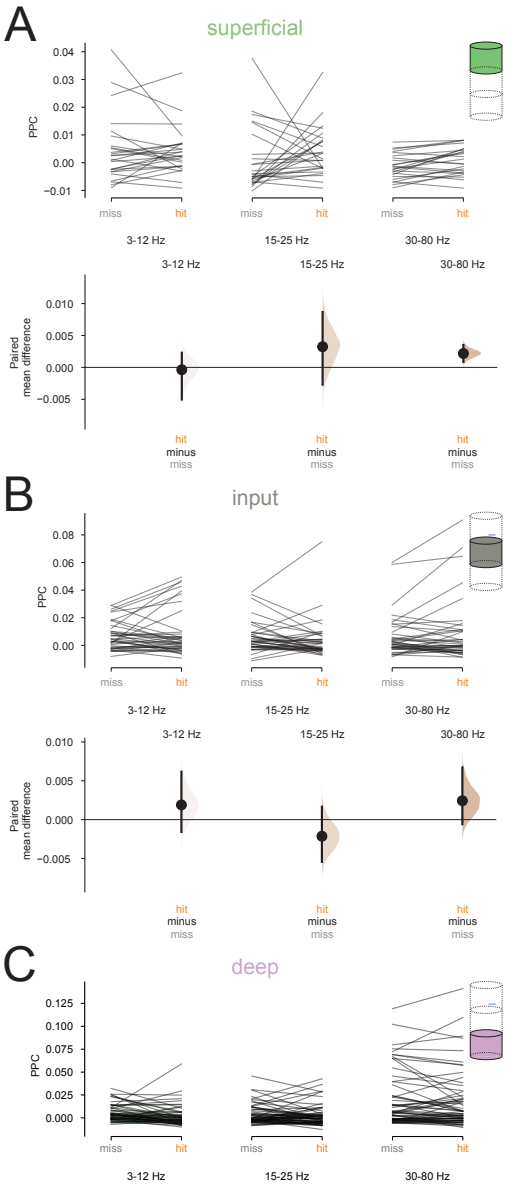

Figure 5-figure supplement 1. Additional PPC data
(**A-B**) Top: Raw PPC values calculated for clusters recorded in the superficial (**A**) and (**B**) input layers in hit and miss trials, averaged into three frequency bands, 3-12 Hz, 15-25 Hz, and 30-80 Hz. PPC was calculated using the LFP recorded on the same channel as the spikes. Bottom: Bootstrapped estimation of the paired mean difference in PPC across hit and miss trials for each frequency band. Note that although there appears to be a difference in high-frequency PPC in the superficial layer, this population does not have significantly positive PPC in either condition, indicating that there is no phase-locking in either hits or misses. (**C**) Raw PPC values for neurons recorded in the deep layer in hit and miss trials, averaged into the same 3 frequency bands. Related to **Figure 5B**.

Figure 5-figure supplement 2

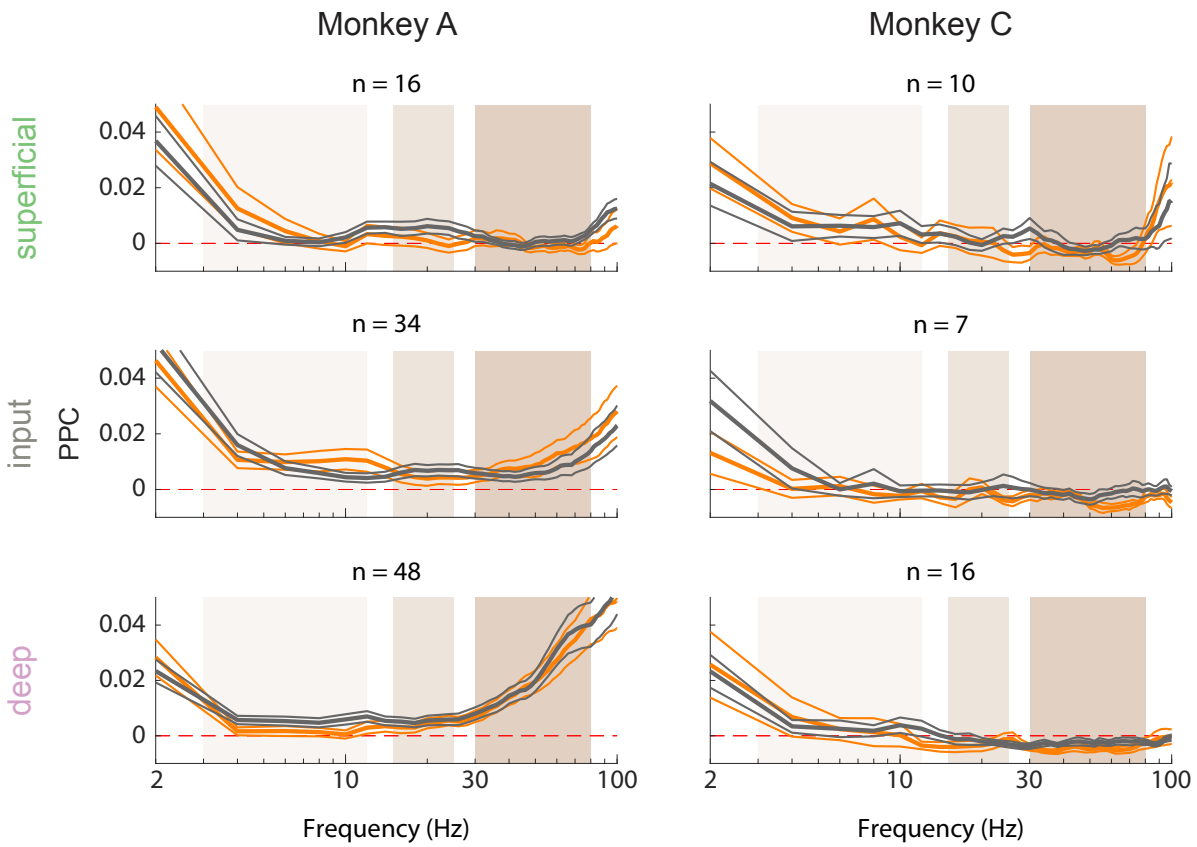

Figure 5-figure supplement 2. Single monkey PPC data
Rows correspond to different layers (top=superficial, middle=input, bottom=deep) and columns correspond to monkeys. Pairwise phase consistency (PPC) of single and multi-units in each layer to the local field potential (LFP) signal recorded from the same channel in hit (orange) and miss (gray) trials at threshold. PPC was calculated in the pre-stimulus period (0-200 ms before stimulus onset). Dashed red line indicates a PPC of 0, below which there is no consistent relationship between spikes and LFP phase.

Figure 7-figure supplement 1

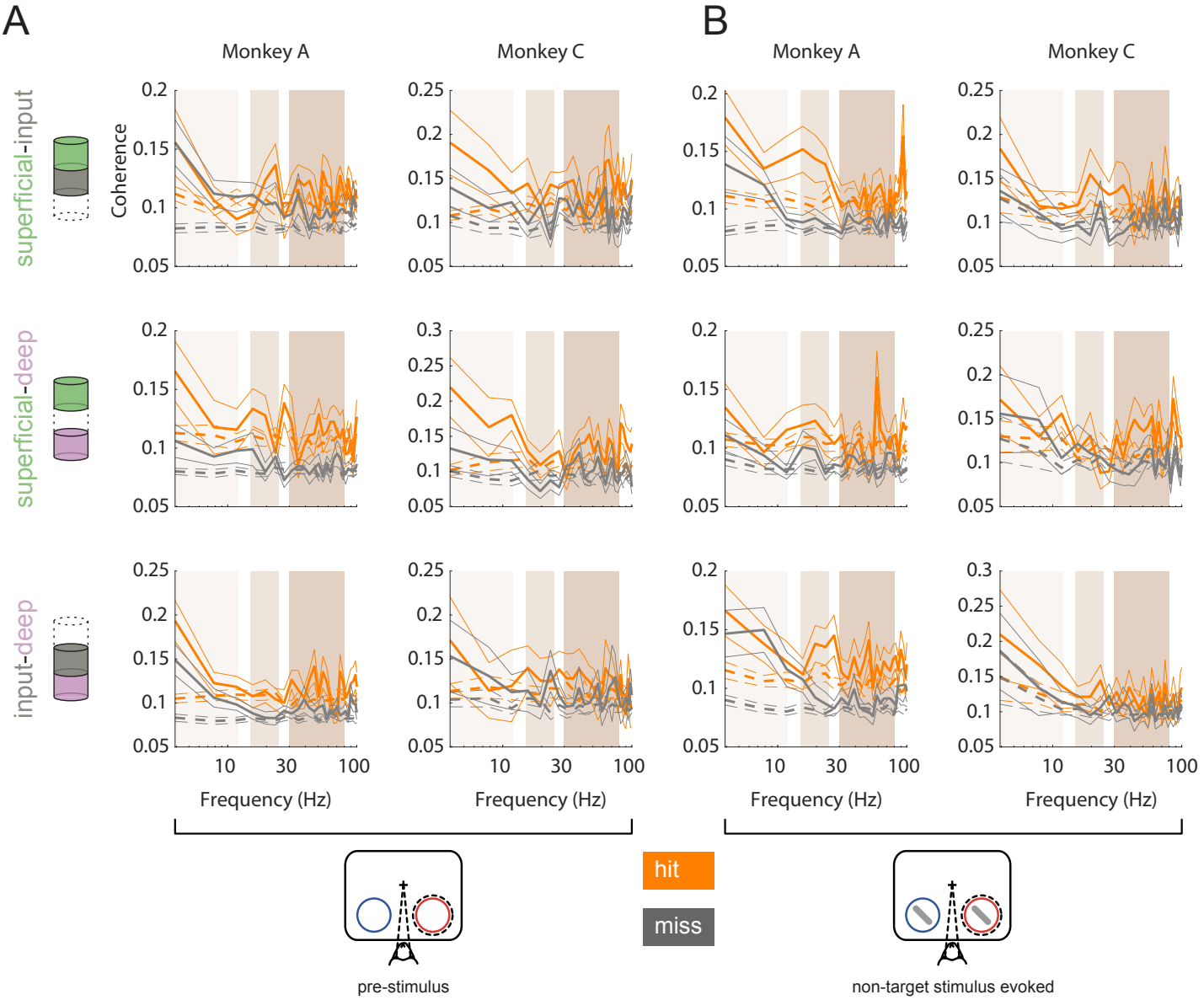

Figure 7-figure supplement 1. Single animal interlaminar coherence
Rows correspond to different pairs of layers (top=superficial-input, middle=superficial-deep, bottom=input-deep). (**A**) Single monkey multi-unit interlaminar spike-spike coherence (SSC) calculated in the 200ms before non-target stimulus onset in hit and miss trials (solid lines, mean +/- s.e.m). Firing rates were matched across hit and miss trials. Dashed lines represent coherence calculated with shuffled trial identities (mean +/- s.e.m). (**B**) Interlaminar spike-spike coherence in the non-target stimulus evoked period in each monkey (60-260ms after stimulus onset). Same conventions as in **A**.

Table 1: Corresponding Null-Hypothesis Testing Results

Result (Figure)	Null-Hypothesis Test	P-Value (Both monkeys)	P-Value (Monkey A)	P-Value (Monkey C)
Pupil diameter (2B)	*t*-test (unpaired)	$p = 6.63624\text{e} - 09$	$p = 1.46705e - 11$	$p = 0.000477729$
Microsaccades (2D)	X^2-test	$p \ll 0.0001$	$p \ll 0.0001$	$p = 3.085882e - 02$
Decoding performance [narrow-spiking] **(3A)**	*t*-test (unpaired) Bonferoni Corrected for 3 comparisons, $\alpha = 0.0166$	Superficial: $p = 1.438522\text{e} - 41$	Superficial: $p = 9.114535\text{e} - 12$	Superficial: $p = 4.86324\text{e} - 39$
		Input: $p = 8.589733\text{e} - 45$	Input: $p = 7.091072\text{e} - 48$	Input: $p = 0.2236990$
		Deep: $p = 1.655900\text{e} - 39$	Deep: $p = 7.422972\text{e} - 31$	Deep: $p = 3.962452\text{e} - 39$
Decoding performance [broad-spiking] **(3B)**	*t*-test (unpaired) Bonferoni Corrected for 3 comparisons, $\alpha = 0.0166$	Superficial: $p = 4.636260\text{e} - 25$	Superficial: $p = 3.171338\text{e} - 13$	Superficial: $p = 1.70382\text{e} - 32$
		Input: $p = 0.2697764$	Input: $p = 0.1658690$	Input: $p = 9.269061\text{e} - 20$
		Deep: $p = 2.755037$e-35	Deep: $p = 5.577542\text{e} - 39$	Deep: $p = 8.339443\text{e} - 14$
Target-evoked firing rate [single and multi-units] **(3E)**	*t*-test (paired) Bonferoni Corrected for 3 comparisons, $\alpha = 0.0166$	Superficial: $p = 4.19108\text{e} - 05$	Superficial: $p = 0.0562592$	Superficial: $p = 0.00174249$
		Input: $p = 1.10838\text{e} - 11$	Input: $p = 0.00072401$	Input: $p = 0.000133564$
		Deep: $p = 1.75826\text{e} - 11$	Deep: $p = 0.00854264$	Deep: $p = 2.32077\text{e} - 05$
Target-evoked firing rate [broad-spiking] **(3F)**	*t*-test (paired) Bonferoni Corrected for 3 comparisons, $\alpha = 0.0166$	Superficial: $p = 0.0526902$	Superficial: $p = 0.0253932$	Superficial: $p = 0.28285$
		Input: $p = 0.000124947$	Input: $p = 6.19734\text{e} - 05$	Input: $p = 0.0122162$
		Deep: $p = 0.00119012$	Deep: $p = 0.00430587$	Deep: $p = 0.0594886$
Target-evoked firing rate [narrow-spiking] **(3F)**	*t*-test (paired) Bonferoni Corrected for 3 comparisons, $\alpha = 0.0166$	Superficial: $p = 0.103689$	Superficial: $p = 0.321259$	Superficial: $p = 0.226899$
		Input: $p = 0.00570757$	Input: $p = 0.0317082$	Input: $p = 0.094339$
		Deep: $p = 0.00393437$	Deep: $p = 0.423418$	Deep: $p = 0.00790649$
Fano Factor modulation index [broad] **(4B)**	*t*-test (unpaired) Bonferoni Corrected for 3 comparisons, $\alpha = 0.0166$	Superficial: $p = 0.0102155$	Superficial: $p = 0.0258056$	Superficial: $p = 0.150999$
		Input: $p = 0.418197$	Input: $p = 0.363723$	Input: $p = 0.889923$
		Deep: $p = 0.708115$	Deep: $p = 0.507158$	Deep: $p = 0.570777$
Fano factor modulation index [narrow] **(S4)**	*t*-test (unpaired) Bonferoni Corrected for 3 comparisons, $\alpha = 0.0166$	Superficial: $p = 0.676039$	Superficial: $p = 0.931029$	Superficial: $p = 0.626767$
		Input: $p = 0.10532$	Input: $p = 0.435288$	Input: $p = 0.164457$
		Deep: $p = 0.950487$	Deep: $p = 0.508305$	Deep: $p = 0.851834$
Deep layer PPC (5B)	*t*-test (paired) Bonferoni Corrected for 3 comparisons, $\alpha = 0.0166$	3-12 Hz: $p = 0.0142$	3-12 Hz: $p = 0.0015$	3-12 Hz: $p = 0.7400$
		15-25 Hz: $p = 0.4064$	15-25 Hz: $p = 0.4875$	15-25 Hz: $p = 0.6515$
		30-80 Hz: $p = 0.3600$	30-80 Hz: $p = 0.5322$	30-80 Hz: $p = 0.1052$

CCA [pre-stimulus, S = superficial, I = input, D = deep] **(6C, left)**	*t-test (paired)* Bonferoni Corrected for 3 comparisons, $\alpha = 0.0166$	I to S: $p = 0.0069$	I to S: $p = 0.0166$	I to S: $p = 0.2329$
		I to D: $p = 0.0287$	I to D: $p = 0.0141$	I to D: $p = 0.9494$
		S to D: $p = 0.0359$	S to D: $p = 0.0107$	S to D: $p = 0.9821$
CCA [stimulus, S = superficial, I = input, D = deep] **(6C, right)**	*t-test (paired)* Bonferoni Corrected for 3 comparisons, $\alpha = 0.0166$	I to S: $p = 0.0021$	I to S: $p = 0.0031$	I to S: $p = 0.3121$
		I to D: $p = 0.0003$	I to D: $p = 0.0001$	I to D: $p = 0.4667$
		S to D: $p = 0.0051$	S to D: $p = 0.0012$	S to D: $p = 0.6522$
SSC modulation index [superficial-input] **(7B, top)**	*t*-test Bonferoni Corrected for 3 comparisons, $\alpha = 0.0166$	3-12 Hz: $p = 0.925338$	3-12 Hz: $p = 0.492935$	3-12 Hz: $p = 0.324414$
		15-25 Hz: $p = 0.107304$	15-25 Hz: $p = 0.47866$	15-25 Hz: $p = 0.0818655$
		30-80 Hz: $p = 0.00394525$	30-80 Hz: $p = 0.0337678$	30-80 Hz: $p = 0.0714013$
SSC modulation index [superficial-deep] **(7B, middle)**	*t*-test Bonferoni Corrected for 3 comparisons, $\alpha = 0.0166$	3-12 Hz: $p = 0.0125919$	3-12 Hz: $p = 0.196645$	3-12 Hz: $p = 0.0163812$
		15-25 Hz: $p = 0.00116552$	15-25 Hz: $p = 0.0035436$	15-25 Hz: $p = 0.113136$
		30-80 Hz: $p = 0.00142568$	30-80 Hz: $p = 0.00111326$	30-80 Hz: $p = 0.192337$
SSC modulation index [input-deep] **(7B, bottom)**	*t*-test Bonferoni Corrected for 3 comparisons, $\alpha = 0.0166$	3-12 Hz: $p = 0.260698$	3-12 Hz: $p = 0.0790771$	3-12 Hz: $p = 0.628428$
		15-25 Hz: $p = 0.0358178$	15-25 Hz: $p = 0.00766517$	15-25 Hz: $p = 0.705241$
		30-80 Hz: $p = 0.0325516$	30-80 Hz: $p = 0.00723361$	30-80 Hz: $p = 0.72298$
SSC modulation index [superficial-input] **(7D, top)**	*t*-test Bonferoni Corrected for 3 comparisons, $\alpha = 0.0166$	3-12 Hz: $p = 0.00344279$	3-12 Hz: $p = 0.00972663$	3-12 Hz: $p = 0.1644$
		15-25 Hz: $p = 3.17111\mathrm{e} - 05$	15-25 Hz: $p = 0.000184256$	15-25 Hz: $p = 0.0559084$
		30-80 Hz: $p = 0.00396824$	30-80 Hz: $p = 0.0243733$	30-80 Hz: $p = 0.0964699$
SSC modulation index [superficial-deep] **(7D, middle)**	*t*-test Bonferoni Corrected for 3 comparisons, $\alpha = 0.0166$	3-12 Hz: $p = 0.0164846$	3-12 Hz: $p = 0.034922$	3-12 Hz: $p = 0.293683$
		15-25 Hz: $p = 0.0890114$	15-25 Hz: $p = 0.0243132$	15-25 Hz: $p = 0.956535$
		30-80 Hz: $p = 0.00441928$	30-80 Hz: $p = 0.050113$	30-80 Hz: $p = 0.0504199$
SSC modulation index [input-deep] **(7D, bottom)**	*t*-test Bonferoni Corrected for 3 comparisons, $\alpha = 0.0166$	3-12 Hz: $p = 0.241036$	3-12 Hz: $p = 0.501995$	3-12 Hz: $p = 0.340605$
		15-25 Hz: $p = 0.00140176$	15-25 Hz: $p = 0.000982425$	15-25 Hz: $p = 0.388365$
		30-80 Hz: $p = 6.84271\mathrm{e} - 05$	30-80 Hz: $p = 0.000141679$	30-80 Hz: $p = 0.149453$
Superficial layer PPC (5-supplement 1B)	*t*-test (paired) Bonferoni Corrected for 3 comparisons, $\alpha = 0.0166$	3-12 Hz: $p = 0.8307$	3-12 Hz: $p = 0.6385$	3-12 Hz: $p = 0.6207$
		15-25 Hz: $p = 0.2812$	15-25 Hz: $p = 0.1918$	15-25 Hz: $p = 0.8869$
		30-80 Hz: $p = 0.0037$*	30-80 Hz: $p = 0.0672$	30-80 Hz: $p = 0.0290$
Input layer PPC (5-supplement 1C)	*t*-test (paired) Bonferoni Corrected for 3 comparisons, $\alpha = 0.0166$	3-12 Hz: $p = 0.3440$	3-12 Hz: $p = 0.2469$	3-12 Hz: $p = 0.1651$
		15-25 Hz: $p = 0.2517$	15-25 Hz: $p = 0.2806$	15-25 Hz: $p = 0.7294$
		30-80 Hz: $p = 0.1881$	30-80 Hz: $p = 0.1045$	30-80 Hz: $p = 0.1725$

* Although this p-value is significant, the PPC in both conditions is below 0, indicating there is no phase-locking in either condition (Vinck et al., 2010).

Table 2: GLM Coefficient Values

Variable (Z-Scored)	Estimated Coefficient	P-Value
Pupil Diameter	0.11754	$p = 0.32869$
Pretarget Microsaccades	-1.3116	$p = 6.0757e - 08$
Target Superficial FR	0.22414	$p = 0.091946$
Target Input FR	0.3276	$p = 0.020068$
Target Deep FR	0.11399	$p = 0.45762$

Table 3: GLM Summary

	Value
Degrees of Freedom	303
Deviance (Full model)	362.8493
Deviance (Excluding microsaccades)	426.5172
Chi^2-statistic (Full model) vs. constant model	65.5
Chi^2-statistic (Full model) vs. constant model p-value	$p = 8.88\mathrm{e} - 13$